Two Classes of Equatorial Magnetotail Dipolarization Fronts Observed by Magnetospheric Multiscale Mission: A Statistical Overview

Soboh Alqeeq, O. Le Contel, P. Canu, A. Retinò, T. Chust, L. Mirioni, A. Chuvatin, R. Nakamura, N. Ahmadi, F. Wilder, et al.

JGR Space Physics

RESEARCH ARTICLE
10.1029/2023JA031738

Key Points:

- We reveal a new class of dipolarization front related to a bump of the magnetic field associated with a minimum in the ion and electron pressures
- The energy conversion process in the S/C frame is driven by the diamagnetic current dominated by the ion pressure gradient
- The energy conversion processes are not homogeneous at the electron scale due to the variations of the electric fields

Supporting Information:

Supporting Information may be found in the online version of this article.

Correspondence to:

S. W. Alqeeq,
soboh.alqeeq@lpp.polytechnique.fr

Citation:

Alqeeq, S. W., Le Contel, O., Canu, P., Retinò, A., Chust, T., Mirioni, L., et al. (2023). Two classes of equatorial magnetotail dipolarization fronts observed by Magnetospheric Multiscale mission: A statistical overview. *Journal of Geophysical Research: Space Physics*, *128*, e2023JA031738. https://doi.org/10.1029/2023JA031738

Received 1 JUN 2023
Accepted 12 SEP 2023

Two Classes of Equatorial Magnetotail Dipolarization Fronts Observed by Magnetospheric Multiscale Mission: A Statistical Overview

S. W. Alqeeq[1], O. Le Contel[1], P. Canu[1], A. Retinò[1], T. Chust[1], L. Mirioni[1], A. Chuvatin[1], R. Nakamura[2], N. Ahmadi[3], F. D. Wilder[4], D. J. Gershman[5], Yu. V. Khotyaintsev[6], P.-A. Lindqvist[7], R. E. Ergun[3], J. L. Burch[8,9], R. B. Torbert[10], S. A. Fuselier[8,9], C. T. Russell[11], H. Y. Wei[11], R. J. Strangeway[11], K. R. Bromund[5], D. Fischer[2], B. L. Giles[5], and Y. Saito[12]

[1]Laboratoire de Physique des Plasmas (LPP), UMR7648, CNRS, Sorbonne Université, Université Paris-Saclay, Observatoire de Paris, Ecole Polytechnique Institut Polytechnique de Paris, Paris, France, [2]Space Research Institute, Austrian Academy of Sciences, Graz, Austria, [3]Laboratory for Atmospheric and Space Physics, University of Colorado Boulder, Boulder, CO, USA, [4]Department of Physics, University of Texas, Arlington, TX, USA, [5]NASA Goddard Space Flight Center, Greenbelt, MD, USA, [6]Swedish Institute of Space Physics, Uppsala, Sweden, [7]Royal Institute of Technology, Stockholm, Sweden, [8]Southwest Research Institute, San Antonio, TX, USA, [9]University of Texas at San Antonio, San Antonio, TX, USA, [10]Space Science Center and Department of Physics, University of New Hampshire, Durham, NH, USA, [11]Department of Earth, Planetary and Space Sciences, University of California, Los Angeles, Los Angeles, CA, USA, [12]Institute for Space and Astronautical Science, Sagamihara, Japan

Abstract We carried out a statistical study of equatorial dipolarization fronts (DFs) detected by the Magnetospheric Multiscale mission during the full 2017 Earth's magnetotail season. We found that two DF classes are distinguished: class I (74.4%) corresponds to the standard DF properties and energy dissipation and a new class II (25.6%). This new class includes the six DF discussed in Alqeeq et al. (2022, https://doi.org/10.1063/5.0069432) and corresponds to a bump of the magnetic field associated with a minimum in the ion and electron pressures and a reversal of the energy conversion process. The possible origin of this second class is discussed. Both DF classes show that the energy conversion process in the spacecraft frame is driven by the diamagnetic current dominated by the ion pressure gradient. In the fluid frame, it is driven by the electron pressure gradient. In addition, we have shown that the energy conversion processes are not homogeneous at the electron scale mostly due to the variations of the electric fields for both DF classes.

1. Introduction

Magnetotail earthward fast plasma flows (Baumjohann et al., 1990) or bursty bulk flows (BBF, Angelopoulos et al., 1992) play a major role in the energy, plasma and magnetic flux transport from the magnetotail to the inner magnetosphere (e.g., Angelopoulos et al., 1994). They are often, although not always (Richard et al., 2022), accompanied by a sharp and transient increase of the northward component of the magnetic field called dipolarization fronts (DFs). DFs are considered as tangential discontinuities (velocity and magnetic field variations are tangential to the front so with no normal component of the magnetic field and no plasma flux flowing through it) separating a relatively cold dense plasma at rest from a hot tenuous plasma in rapid motion (e.g., H. S. Fu et al., 2012a; Sergeev et al., 2009). The origin of the fast flows and their related DFs is still a matter of debate. The main formation mechanisms currently studied are magnetic reconnection (e.g., Drake et al., 2014; Sitnov et al., 2009), kinetic ballooning interchange instability (e.g., Panov et al., 2022; Pritchett & Coroniti, 2010) and low entropy magnetic flux tubes (e.g., Pontius & Wolf, 1990; Wolf et al., 2009). Fast plasma flows and DFs can be related to a global scale substorm activity or appear as isolated structures. Regarding the spatial scale of DFs, R. Nakamura et al. (2004) investigated spatial gradients of high-speed flows in the mid-tail plasma sheet using multi-satellite Cluster observations (Escoubet et al., 2001). They found that the typical scales of fast flows/BBFs are about 2–3 R_E in the dawn-dusk direction and 1.5–2 R_E in the north-south direction. Using THEMIS data (Angelopoulos, 2008), J. Liu et al. (2013) also estimated the dawn-dusk size of dipolarizing flux bundles (localized areas of dipolarized flux tubes) between 1 and 3 R_E. These scales can be considered as upper limits for DFs which correspond to the flow front or can be embedded in these fast flows. Along the direction of propagation, the DF thickness was shown to be about a few ion inertial lengths (e.g., Runov et al., 2009; Schmid et al., 2011).

Runov et al. (2011) summarized the general characteristics of DFs as an asymmetric bipolar variation of the northward component of the magnetic field associated with ion density and pressure decrease and ion temperature increase after the DF passage. However, DFs can be represented in different categories. Schmid et al. (2015) discussed four categories of DFs. They performed a statistical study of the temperature and density variations during DF crossings, using 9 years (2001–2009) of Cluster data. They found ∼54% of DFs belonging to the category A defined by a temperature increase while the density and the thermal pressure decrease across the DF. The second most important category B (28%) corresponds to an increase of the density while the temperature decreases and the thermal pressure shows no significant change; it is also associated with slower plasma flow and larger background northward magnetic field component than category A. Based on these results, the authors suggested that fast flows could be generated by reconnection in the magnetotail producing DFs of category A. Then the latter could evolve into a DF of category B during their earthward propagation toward the braking region. Following this first study, Schmid et al. (2019) identified two DF subcategories depending on the sign of the magnetic field dip preceding the DF. A positive dip was found to be correlated with the enhancement of the perpendicular and diamagnetic currents flowing ahead of the DF. A negative dip was more correlated with field-aligned currents and was suggested to be related to flux ropes and/or resulting of localized guide field reconnection. It has been suggested that the formation of this dip ahead of the DF was due to the interaction of background ions with the earthward moving front. Indeed, modeling the DF as a convex structure, X.-Z. Zhou et al. (2014) showed that the ion acceleration by the duskward electric field of the DF and then their reflection can lead to an increase of the dawnward current causing the B_z dip. Later, Pan et al. (2015) carried out a statistical study using THEMIS data and found consistent results. In addition, they showed that the depth of the B_z dip is larger for DF with higher speed.

DFs host different mechanisms of particle acceleration (see H. Fu et al., 2020, for a review) and are thought to play an important role in the magnetosphere global energy cycle. Due to the enhancement of the cross-tail current at DF and the motional electric field, energy is dissipated along their earthward propagation. It was suggested that this dissipation is due for a major part to the Ion reflection at DF (J.-Z. Li et al., 2016). Depending on assumed DF sizes in the azimuthal and vertical directions a significant energy dissipation occurs (e.g., Angelopoulos et al., 2013). Various statistical studies have been performed about the energy conversion rate $\mathbf{J}\cdot\mathbf{E}$ associated with DFs (where $\mathbf{J}$ is the current density and $\mathbf{E}$ the electric field). Using Cluster data, Hamrin et al. (2014) found that fast flows with a velocity peak behind the front (equivalent to a growing Flux Pileup Region FPR as introduced by H. S. Fu et al. (2012b)) were decelerated and energy was radiated, that is, converted from particles to fields. For fast flows with velocity peak detected ahead or at DF (decaying FPR as introduced by H. S. Fu et al. (2012b)), no braking signature was detected and energy was dissipated i.e., transferred from fields to particles. Also from Cluster statistical data analysis, Huang et al. (2015) found that the energy was significantly dissipated at DFs. More recently and using the high temporal and spatial resolutions of Magnetospheric Multiscale mission (MMS) data (Burch et al., 2016), Zhong et al. (2019) analyzed 122 DFs gathered from May to August 2017 and found that the electromagnetic energy is mostly transferred to plasma at DF ($\mathbf{J}\cdot\mathbf{E} > 0$). In the fluid frame, they found that $\mathbf{J}\cdot\mathbf{E}' = \mathbf{J}\cdot(\mathbf{E} + \mathbf{v}_e \times \mathbf{B})$ could be positive and negative but on average it is very small. Khotyaintsev et al. (2017) compared Cluster observations with results from 3D Particle-In-Cell (PIC) simulations. They concluded that the energy dissipation in the satellite frame was mainly due to the motional electric field and the ion contribution to the cross-tail current density. No significant energy conversion was found in the DF frame (defined by using the ion velocity at the DF). Portioning of the energy at DFs between ions and electrons was investigated by Sitnov et al. (2018) using kinetic energy dissipation parameter introduced by Y. Yang et al. (2017). Ions were heated at and ahead of DFs, whereas electrons were heated at and behind due to the long-wavelength Lower-Hybrid Drift (LHD) instability (LHDI). Therefore, it was suggested that both contributions lead to an important energy dissipation. However, such an analysis applied to in situ MMS data did not provide clear signatures (Zhong et al., 2019). Still from 3D PIC simulations, T. K. M. Nakamura et al. (2019) reported energy dissipation within the density gradient layer at DF (in the fluid frame) due to the LHDI.

Alqeeq et al. (2022) investigated in detail six DF events observed by MMS in the Earth's magnetotail on 23 July 2017. The energy conversion processes were also analyzed based on the calculation of the $\mathbf{J}\cdot\mathbf{E}$ term. They found that, in the frame of the satellite, the energy is dissipated (dissipation or load region) ahead of the DF but transferred from the plasma to the fields behind the front (dynamo or generator region). This inversion is caused by the inversion of the current density as the motional electric field does not change sign during the DF crossing. In the fluid frame, the energy was found to be transferred from the plasma to the fields as

also found in a previous MMS single DF event (Z. H. Yao et al., 2017). This dynamo region could contribute to the slowdown of the fast flow. Then, by calculating the standard deviation (SD) of the current density and the electric field measurements from the four satellites, they found that this energy conversion is not homogeneous at the electron scale due to the electric variations produced by the electron pressure gradient. The LHD waves have been suggested as a possible source of these electric field variations although due to the time averaging of all data (0.3 s), the high-frequency part of the spectra was filtered out. These waves are expected to be generated by the large density gradient at DFs (e.g., Divin et al., 2015a; Hosner et al., 2022; Le Contel et al., 2017; C. M. Liu et al., 2018; Sergeev et al., 2009; J. Yang et al., 2017) generating ripples on the front at the electron scales and thus leading to the non homogeneity of the energy conversion process (Pan et al., 2018).

In order to extend these case study results, we have carried out a statistical study of the energy conversion processes at DFs using MMS observations from the full 2017 magnetotail season. Based on this statistical investigation, we show that two subclasses of DF can be distinguished depending on the magnetic field profile and sign of the energy conversion term. These two subclasses, although sharing some common properties with Schmid et al. (2019) subcategories, are not identical. We also confirm the non-homogeneity of the energy conversion processes at electron scales. The present study is organized as follows: data, methods and event selection are described in Section 2, and an overview of the statistical DF properties is presented in Section 3. In Section 4, we present cross-validation of current density calculations, ion and electron dynamics are investigated thanks to the Ohm's law in Section 5, then the energy conversion processes in the vicinity of DFs are scrutinized in Section 6. The global results of this statistical study are summarized and discussed in Section 7. Finally, we conclude in Section 8.

2. Data, Methods, and Event Selection

2.1. Data and Selection Criteria

Data used for this statistical study are provided by the following MMS instruments: the Fluxgate Magnetometer (FGM) in burst mode (Russell et al., 2016), the Electric Double Probe in fast survey mode (Ergun et al., 2016; Lindqvist et al., 2016), the Fast Plasma Instrument (FPI) (Pollock et al., 2016), and the Hot Plasma Composition Analyzer (HPCA) (Young et al., 2016).

We have selected DFs using burst FGM and FPI (DIS and DES) nominal L2 data in *GSE* from the full magnetotail season of 2017 (end of April to end of August). In order to automatically identify DF signature, we have used an Artificial Intelligence Data Analysis (AIDApy) routine (Lapenta & AIDA H2020 Team, 2019) based on the difference between maximum and minimum values of physical quantities (n, Vi, B, …) computed within a 60 s sliding window. A typical DF signature is defined by the following:

- an increase of the northward B_z component of the magnetic field >6 nT,
- an increase of the X component of the ion velocity >150 km/s,
- an increase of both parallel and perpendicular temperatures of ions (>5) and electrons (>1 keV),
- a decrease of both ion and electron densities (only corresponding to a negative value of the difference between maximum and minimum values without specific threshold value).

This first automatic selection step provided 857 DF events. The following constraints are checked manually:

- Electron partial moment data have to be available at least 60 s before and 60 s after DF crossing. DF crossing time t_0 is defined by the maximum of B_z in the selected time interval.
- Only DFs near the Earth's magnetotail equator are kept using the following constraint $|B_x| < 5$ nT.

Indeed, electron partial moment data computed by the FPI team are necessary due to the very low density values (and low counts) in the magnetotail (see Alqeeq et al. (2022), for more details). Due to these constraints, the new DF list is reduced to 132 DF events. These criteria are quite similar to those used in previous DF statistical studies (e.g., H. Li et al., 2015; J. Liu et al., 2013; Zhong et al., 2019). For instance, Zhong et al. (2019) limited their DF selection by considering only plasma densities between 0.2 and 0.9 p cm^{-3} and burst mode data available at least 15 s before and 30 s after the DF. On the other hand, J. Liu et al. (2013) considered just the measurements in the magnetotail region defined by $-30\ R_E < X_{GSM} < -6\ R_E$ whereas H. Li et al. (2015) investigated the region defined by $X_{GSM} \leq -8\ R_E$ and $|Y_{GSM}| \leq 10\ R_E$.

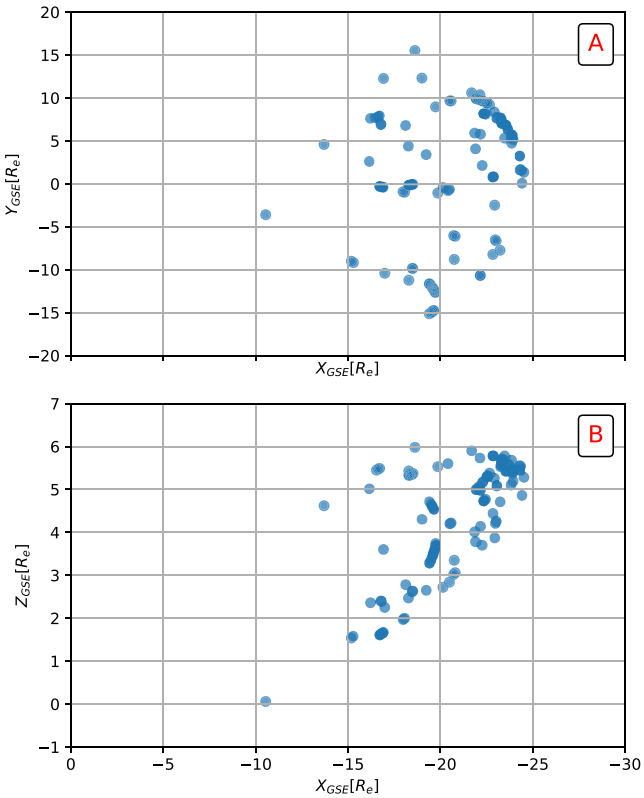

Figure 1. An overview of all dipolarization fronts (DFs) events that match the selection criteria. Panels (a) *XY* and (b) *XZ* position of Magnetospheric Multiscale mission during the observations of the 132 DF events in *GSE*.

In the present study, the selection criteria are applied to each spacecraft and only events observed by all four MMS satellites are kept. Finally, all selected DF events have been individually validated by a visual check.

Figures 1a and 1b, show that all selected DFs are located in the region satisfying $-25 \leq X_{GSE} \leq -10$ R_E and $|Y_{GSE}| \leq 15$ R_E. The DF distribution is quite symmetric in the equatorial plane while it is shifted toward the north mostly due to the seasonal effect (inclination of the rotation axis of the Earth's toward the Sun during the North hemisphere summer) (see Figures 2a and 2b). The external limit at $X_{GSE} \sim -25$ R_E corresponds to the MMS apogee in 2017. The internal limit at $X_{GSE} \sim -10$ R_E is a bit farther from the Earth than the beginning of the fast survey mode associated with the Region Of Interest (ROI) ($X_{GSE} < 9$ R_E). Therefore the outer and inner limits are related to the MMS apogee and ROI and do not mean that DF cannot be detected nearer or farther from the Earth.

2.2. Methods

DFs are characterized as a sharp increase of the northward component of the magnetic field B_z which are generally preceded by a short decrease, a dip (e.g., Huang et al., 2015; Runov et al., 2009; Schmid et al., 2015; Sergeev et al., 2009; Zhong et al., 2019). DF signatures are usually displayed in a local coordinate system obtained from a Minimum Variance Analysis (Sonnerup & Scheible, 1998) applied on magnetic fields data MVAB of a single spacecraft (e.g., Huang et al., 2015; C. M. Liu et al., 2018) and/or from a timing analysis (TA) in case of multi-spacecraft missions (e.g., H. S. Fu et al., 2012b).

In the present study, MVAB is applied on the four spacecraft average of the magnetic field during the time period corresponding to the sharp increase of northward component B_z (defined as the period between the minimum and the maximum values) for all selected DF events. As MMS satellites are separated at electron scales and DF thickness and width are about a few ion inertial lengths and 2–3 R_E respectively, MVAB applied on each single spacecraft magnetic field data gives similar *LMN* frames. *LMN* coordinates are well defined and correspond to *L* directed northward, *M* approximately directed dawnward, and *N* approximately directed Earthward. The time periods used to perform MVAB and its results are found in Supporting Information S1.

From these MVAB results, we define *L*, *M*, and *N* vectors as maximum, intermediate, and minimum variance directions respectively. We have verified that the ratio between the three corresponding eigenvalues, λ_1, λ_2, λ_3 are sufficiently large (average values of the ratio $\lambda_M/\lambda_N \sim 22.034$ and of the ratio $\lambda_L/\lambda_N \sim 420.13$, lowest ratio value is 2.) indicating that the three directions are well separated.

The components of the normal vector are estimated by a TA as well as the speed along the normal (these results can be found in Supporting Information S1). Note that in accordance with the propagation direction given by TA, the orientation of the *N* vector of the MVAB was set to be positive (earthward) and *L* always oriented northward leading to *M* directed dawnward.

Figures 3a–3d show the histogram for each component of the normal vector (from TA and MVAB methods) as well as the magnitude of the normal speed obtained by TA. While all DFs are propagating earthward, percentages indicate that duskward/dawnward and northward/southward DF propagations are relatively balanced with no specific statistically significant direction. Figure 3g shows a peak of the speed histogram around 200 km/s. The smallest values below 50 km/s correspond to a normal orientation almost perpendicular to the *X* axis when DFs are crossed through their flanks. In such a configuration, the DF speed can be much slower than the radial fast flow propagation.

In the present study, Superposed Epoch Analysis (SEA) are performed using the State Estimation and Analysis in Python (SeaPy). Time series have been reorganized by setting the maximum of the magnetic field as a reference

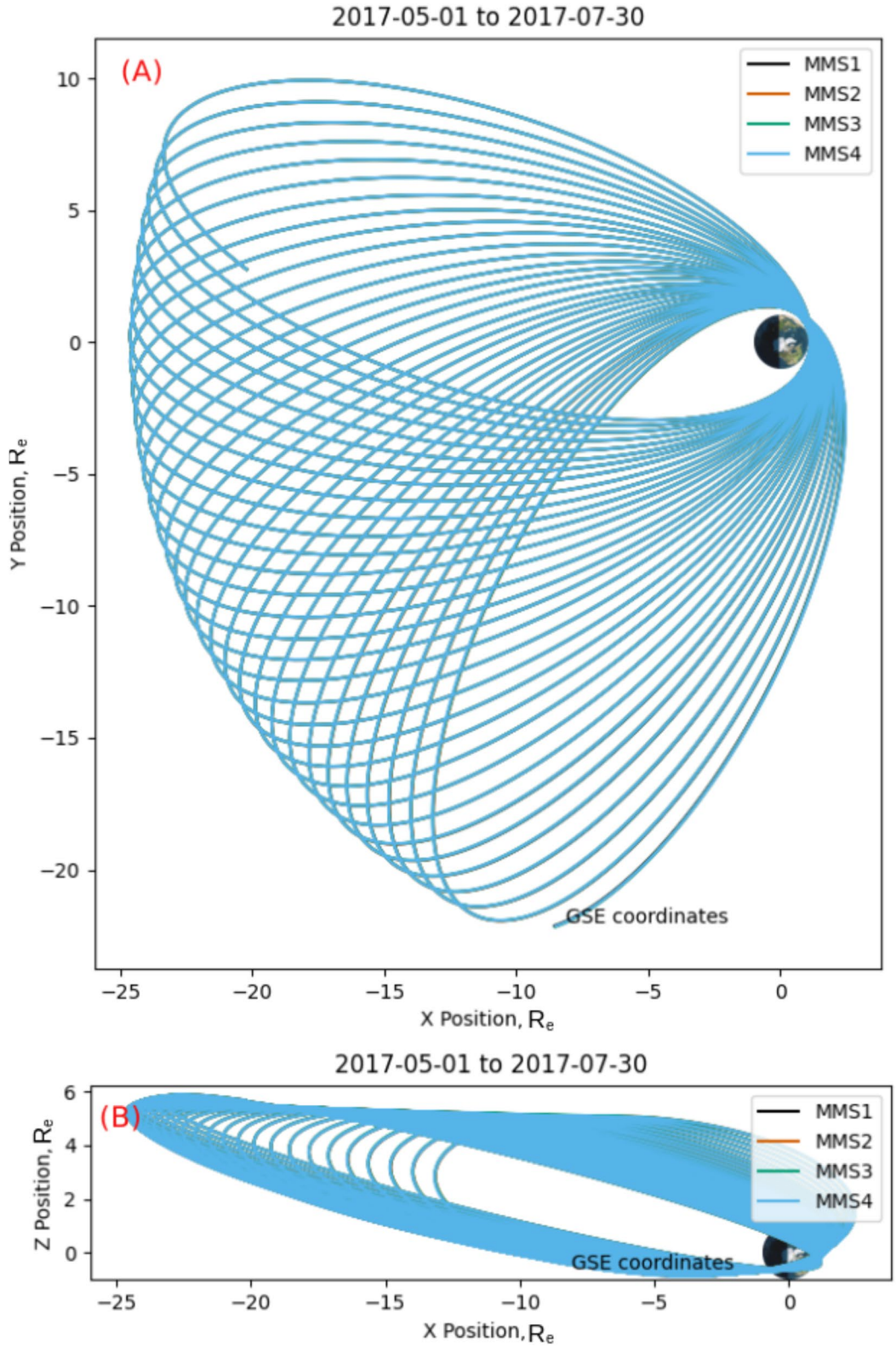

Figure 2. Magnetospheric Multiscale mission (MMS) orbit for the magnetotail season from 2017 (1 May to end of July in *GSE* frame. Panel (a) shows MMS orbit in *XY* plane and (b) in *XZ* plane. Not that at these global scales, individual MMS orbits are superposed as the satellites are separated at electron scales.

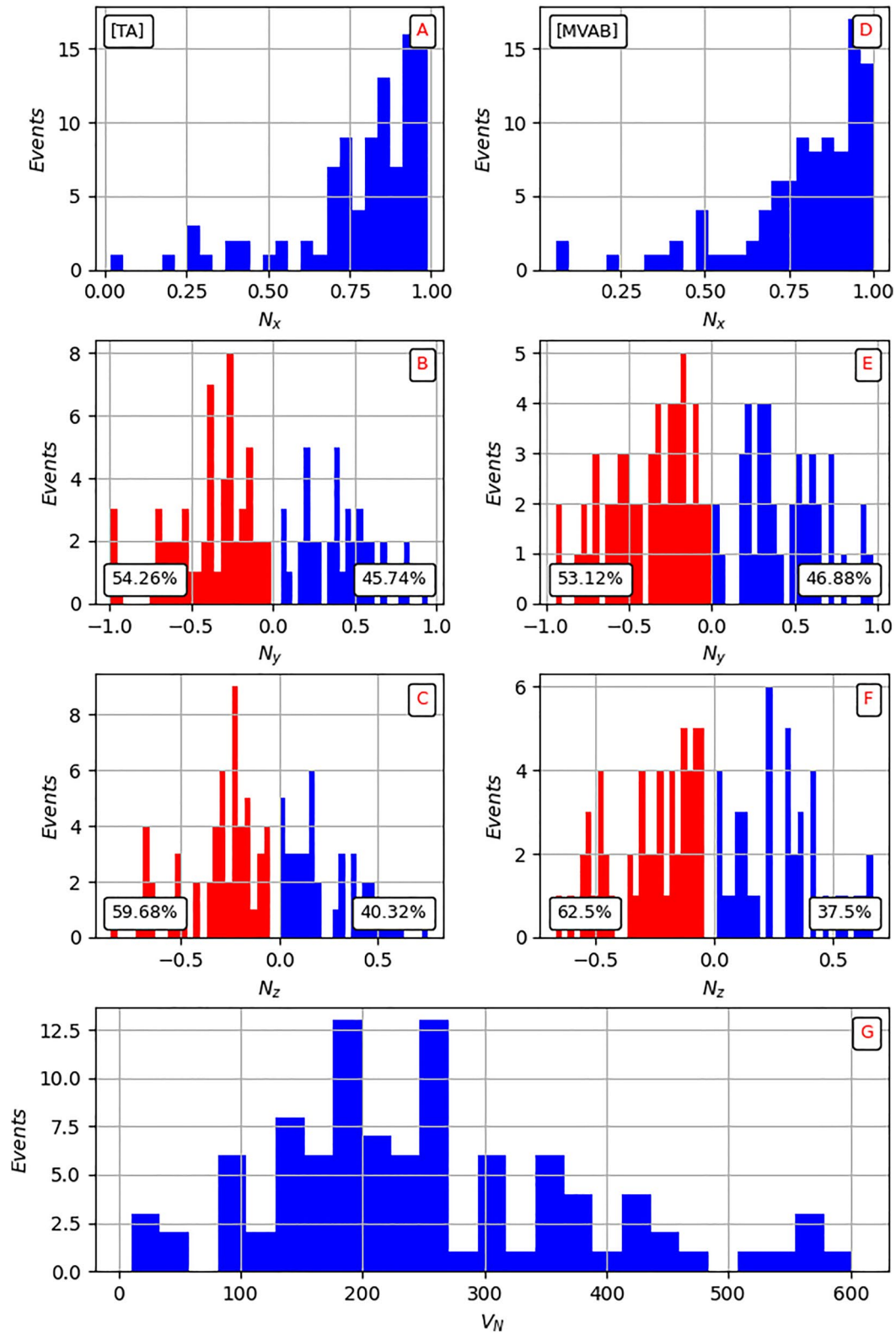

Figure 3. Histograms of the normal components in *GSE*, from timing analysis (TA) panels (a–c) and from MVAB panels (d–f). Panel (g) shows the magnitude of the normal velocity obtained by TA.

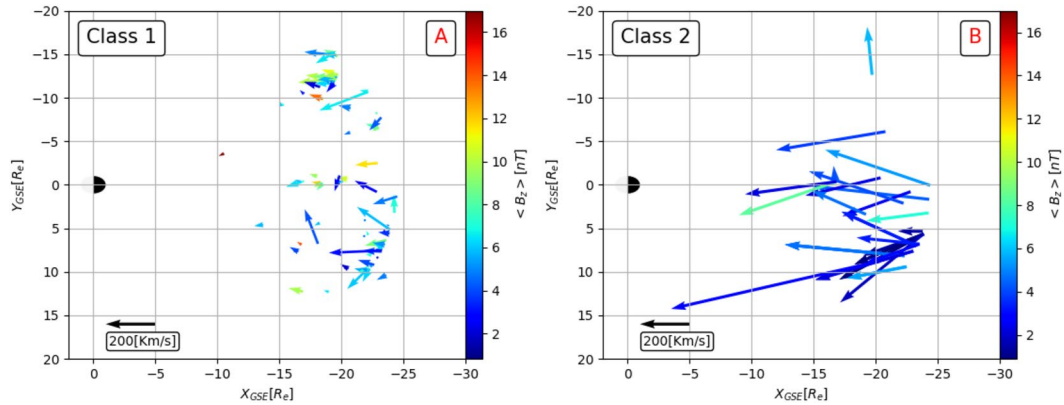

Figure 4. Superposed epoch analysis plots of dipolarization front (DF) signatures using 132 DFs, in their respective *LMN* frame, all data being time averaged at 0.3 s. In each panel, the black line marks the superposed epoch median, the red dashed line marks the superposed epoch mean, and the blue fill marks the interquartile range. (a) Magnetic field B_L, (b) electron density N_e, (c, d) electron and ion pressures from Fast Plasma Instrument (FPI), (e) Hot Plasma Composition Analyzer (HPCA) proton temperature T_{H^+}, (f, g) perpendicular electron T^e_{perp} and ion T^i_{perp} temperatures from FPI, (h) HPCA normal proton bulk velocity V_{H^+N}, and (i) FPI normal ion bulk velocity vi_N.

for the measurements t_0 and the duration of a time period (t_{0-180}, t_{0+180}). The mean, the median and the interquartile range are computed. Note that the median measure is less impacted by departures from normality (Morley et al., 2014).

3. Statistical Overview of Classical DF Properties

In this section, we describe the results obtained using a SEA described in Section 2, where we defined the representative time series by setting the maximum of B_L component of the magnetic field as a time reference for the measurements and we kept 180 s of data on each side of this time reference. Furthermore, each DF data is time averaged at 0.3 s in order to remove all fluctuations which are not consistent with the phenomenon time scale.

After the first SEA using the full set of DFs, we realized that an important dispersion was due to the existence of two different types of magnetic signatures satisfying the DF selection criteria but having different time scales. From this observation, we decided to split the DF set into two different classes based on t_{DF} the time between the minimum and the maximum of the B_L component of the magnetic field at the front, also used to calculate the MVAB and determine the front normal. Thus, a DF event belongs to class I for $t_{DF} > 5$ s or to class II for $t_{DF} < 5$ s, 5 s being of the order of the ion gyroperiod in a 12 nT background magnetic field. Then we perform two separate SEAs. The statistical characteristics of DF events for these two different classes are shown separately, reducing the dispersion for each class.

Figure 4 shows SEA results in order to illustrate ion scale properties for both DF classes in their respective *LMN* frame obtained from MVAB. Figure 4a presents the most important DF characteristics; namely a sharp increase of the northward component of the magnetic field B_L showing a small decrease (dip) just before the front as reported by previous studies (e.g., C. M. Liu et al., 2018; Ohtani et al., 2004; Panov et al., 2022; Runov et al., 2009; Schmid et al., 2015; Z. Yao et al., 2013; Z. H. Yao et al., 2015). Figure 4b shows the decrease of the electron density N_e to 0.21 p cm^{-3}. Figures 4c and 4d display electron and ion pressure variations respectively. For electrons as well as for ions, the DF crossing always corresponds to a transition between a high pressure to a low pressure region on the largest scale (fluid). Figures 4f and 4g present the perpendicular electron and ion temperatures from FPI data in order to compare with proton temperature from HPCA data Figure 4e. Due to their different upper energy limit 40 keV (resp. 30 keV) for HPCA (resp. for FPI-DIS), FPI-DIS ion moments, although having a faster time resolution, can be underestimated. Indeed, a comparison of Figures 4g and 4e confirms that isotropic HPCA proton temperatures are much larger than FPI perpendicular ion temperatures (adding parallel ion temperatures to compute isotropic FPI temperatures does not compensate for the discrepancy, not shown). For the same reason, HPCA proton velocities $V_{H^+,N}$ are much larger than FPI ion velocities V_N as shown in Figures 4h and 4i. The V_N decreases shown by FPI-DIS within the front when ions are energized can also be considered as an artifact caused by this limited upper energy and not as a real reduction of the fast flow velocity.

Class I corresponds to 74.4% of selected DFs and has typical DF properties reported so far by previous statistical studies (e.g., Huang et al., 2015; Ohtani et al., 2004; Schmid et al., 2015, 2019; Zhong et al., 2019). This DF class displays a slow decrease of the magnetic field after the front (see Figure 4(class I-[A])) and is associated with a lower ion velocity than class II (see Figure 4(class I-[H] and class II-[H])). They seem to propagate through a hotter plasma as ion and electron temperatures are higher before the front than for class II (see Figure 4(class I-[E,F,G] and class II-[E,F,G])). The ion perpendicular temperature increase is smaller whereas a significant (∼50%) electron perpendicular temperature increase is present. Yet, both pressures decrease monotonously at the DF (Figure 4(class I-[C,D]). This class is very similar to the decaying field pile-up event defined by H. S. Fu et al. (2012b) although it is not clear that the peak of the velocity is colocated with the DF.

Class II corresponds to 25.6% of selected DFs. This new DF class has the same time scale for the rising and the falling of B_L (like a bump) (see Figure 4(class II-[A])) associated with minimums of density and (ion and electron) pressures (see Figure 4(class II-[B-D])). In addition to the pressure minimums at DF crossing, compressional fluctuations with smaller amplitudes are present. This DF class has larger velocity than class I (see Figure 4(class I-[H] and class II-[H])). One can notice that the level of fluctuations in Class II events is higher than in Class I. These fluctuations cannot be removed by increasing the time average, as we are limited by the need to resolve the short DF time scale of a few seconds. They are likely related to the development of turbulence which could be caused by the larger speed of class II events leading to stronger shear flows (e.g., Ergun et al., 2015; Stawarz et al., 2015). As the $V_{H^+,N}$ maximum is located behind the front, this class could correspond to the growing field pile-up event defined by H. S. Fu et al. (2012b). However, for class II the increase of the velocity continues after the end of the pile-up region (end of the bump) whereas it is confined inside the pile-up region in H. S. Fu et al. (2011) and H. S. Fu et al. (2012b) events. Furthermore, the difference of time resolution of particle measurements between Cluster (4 s) and MMS (here 0.3 s after time averaging) do not allow to know if the minimum of particle pressures, occurring within a few seconds, is also detected for growing FPR studied by H. S. Fu et al. (2011) and H. S. Fu et al. (2012b). As already mentioned, these DF events seem to propagate through a colder plasma than class I as ion and electron temperatures before the front are smaller. Finally, both ion and electron perpendicular temperatures increase significantly (∼50%). It is worth noting that this DF class is mostly detected on the duskside and includes all six DF events analyzed in Alqeeq et al. (2022) (see Figure 5(class II)). Substorm onsets being also more frequent in this region, it could suggest a possible link between the two phenomena.

Figure 5 displays an overview of class I and class II events that match the selection criteria. The colors represent the change in the northward magnetic field component $< B_z >$ averaged over the full DF time interval, the arrows represent the DF normal speed perpendicular to the boundary (obtained by TA) projected onto the *XY* plane in *GSE*. While for class I, locations and propagations are relatively random, class II DFs have preferentially duskward locations and propagations with larger speeds. The colors represent the change in the northward magnetic field component $< B_z >$ averaged over the full DF time interval (defined as 75 before and 75 s after t_0).

Finally, Figure 6 shows that both classes are detected more frequently farther from the Earth (∼24–25 R_E). However, class I DF events can be also detected closer to the Earth down to 12 R_E while class II are only detected at farther distances.

Schmid et al. (2019) also identified two subcategories of DFs based on the sign of the magnetic dip preceding the DF. This dip property also permits us to distinguish between our two classes as class I shows an average and median positive B_L dips whereas class II shows slightly negative values (see Figure 4a). The histogram of the radial distance of our two DF categories, although more extended in distance from 12 to 26 R_E, is globally consistent with theirs (see Figure 5 of Schmid et al. (2019)) where they found that positive dip DF category is detected closer to the Earth (∼18 R_E) than negative category (∼26 R_E). However, we do not find a decrease of the occurrence of the class I with the increase of the radial distance from the Earth. Furthermore, our class II has a larger median speed by a factor 2 than class I while Schmid's negative DF-dip subcategory has only a larger median speed by 50% than the positive DF-dip subcategory. Finally, the bump profile of our class II is not found for the Schmid's negative dip DF subcategory. Therefore, although sharing common properties, these two subclasses do not seem to be identical.

4. Currents Density Structure Associated With DF

Following the same approach as for analyzing the first six DF events described in Alqeeq et al. (2022), we have compared the current densities computed from ion and electron moments averaged over the four individual

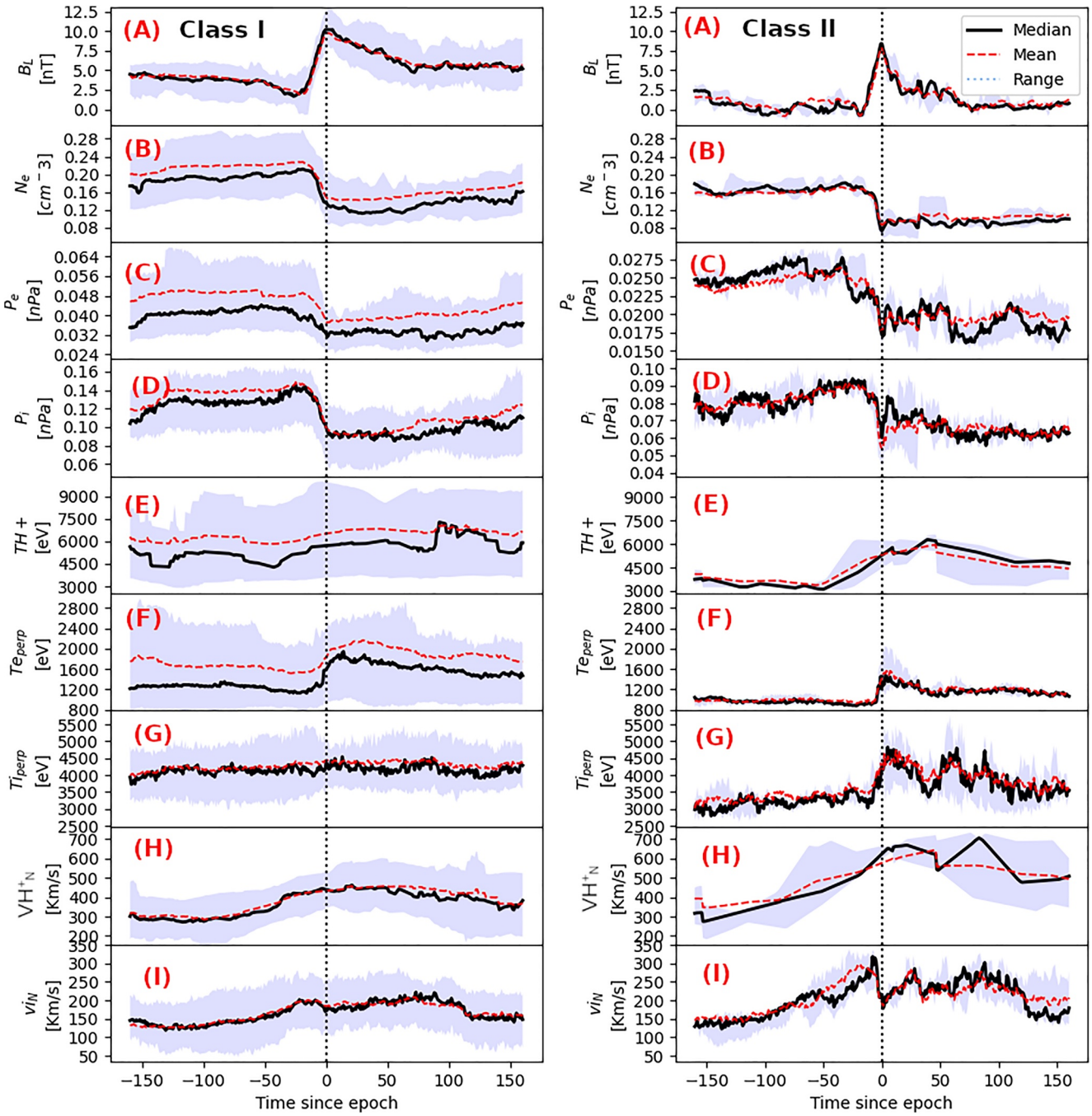

Figure 5. An overview of class I and class II events that match the selection criteria. The colors represent the change in the northward magnetic field component $< B_z >$ time averaged over the full dipolarization front (DF) time interval, and the arrows represent the DF velocity perpendicular to the boundary (obtained by timing analysis), projected onto the *XY* plane in *GSE*.

spacecraft with those estimated independently from the magnetic field data at the same time resolution (0.3 s) using the curlometer technique (e.g., Chanteur & Harvey, 1998).

Figure 7 shows the SEA of the current densities computed from particle measurement $\mathbf{J}_{part} = en_e(\mathbf{v}_i - \mathbf{v}_e)$ (Figure 7e) and computed from the magnetic field $\mathbf{J}_{\text{curl}} = (\nabla \times \mathbf{B})/\mu_0$ (Figure 7d) estimated for each DF event in their own *LMN* frame. For both categories, the comparisons demonstrate good agreements between the two current density measurements although the values are quite small (~ -6 nA/m^2). Note that each DF can be identified by its negative peak in J_M (an increase of cross-tail duskward current).

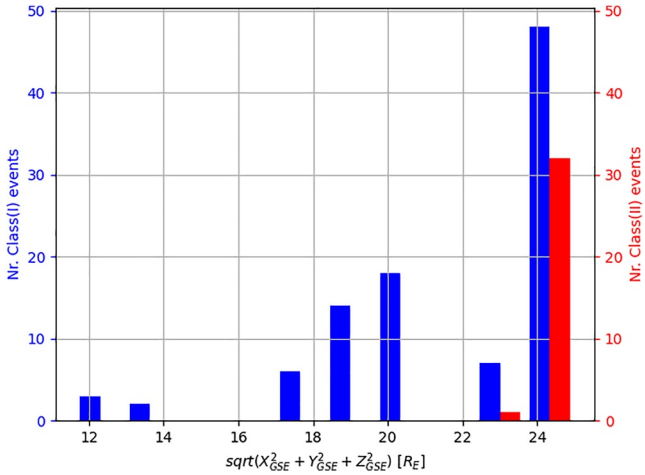

Figure 6. Histogram of the radial distance of the dipolarization front observation location. The red bars represent class(II) and the blue bars the class(I).

In addition to these measured current densities, one can obtain, from two-fluid theory, the diamagnetic current densities computed from the electron and ion pressure gradients. Due to the very low density in the magnetotail, the full divergence of the pressure tensor is very noisy and not reliable. However, these gradients along the DF normal can be estimated by a single satellite method by converting time evolution to distances using the DF speed obtained by TA: $\partial_t P = \partial_N P_{i,e} \cdot V_N$. The M component of the total (perpendicular) diamagnetic current density becomes $J_{dia-tot,M} = B_L/B^2 \nabla_N (P_e + P_i)$ (where all data are averaged over the four satellites) and can be compared with the two other current densities computed from particle moments and curlometer technique.

Figures 7a–7c show the electron diamagnetic current $J_{dia-e,M} = B_L/B^2 \nabla_N P_e$, the ion diamagnetic current $J_{dia-i,M} = B_L/B^2 \nabla_N P_i$, and the total diamagnetic current $J_{dia-tot,M} = B_L/B^2 \nabla_N (P_e + P_i)$ along the M direction, respectively. From the comparison between ion and electron diamagnetic currents, we see that for both classes the ion contribution is dominant and constitutes $\simeq$72% of the total diamagnetic current. Furthermore, for both classes, the total diamagnetic current along M is highly consistent with the curlometer and particle measurements indicating that the diamagnetic effect is the main source of the current. More importantly, the systematic and significant reversal in the current density pointed out in Alqeeq et al. (2022) as the cause of the reversal of the energy conversion process for the six analyzed DF events is confirmed by this statistical study as being a common signature of class II events. Although being small, we point out that the positive peak of the reversal of the current density after the DF crossing is obtained by three independent measurements (i.e., from pressure measurements (J_{dia}, Figure 7c), magnetic field measurements (J_{curl}, Figure 7d) and density and velocity measurements (J_{part}, Figure 7e)). Consequently, it can be considered as a reliable signature and not due to random variations of the current density. Finally, this statistical study demonstrates that the reversal of the current density for class II events is mainly due to the reversal of the ion pressure gradient or in other words by the ion diamagnetic current. Although the electron density gradient follows the same behavior, the electron pressure gradient is smaller mainly due to their smaller temperature. Therefore for both DF classes, the perpendicular current density structure of DF is governed by the diamagnetic current density dominated by the ion gradient pressure produced by the propagation of the fast flow through the magnetotail.

5. Statistical Analysis of Ohm's Law

In this section, we reproduce the analysis of the different terms of the generalized Ohm's law for our two different DF classes. Figure 8 shows for both categories the SEA of the ideal ion frozen-in ($\mathbf{E'^i} = \mathbf{E} + \mathbf{v}_i \times \mathbf{B}$) and the Hall electric field ($\mathbf{J}_{part} \times \mathbf{B}/(en)$) terms in LMN coordinates. For instance for class II, we can check that the Ohm's law along N is satisfied as the mean values corresponding to red dashed lines give E'^i_N (~3 mV/m, Figure 8d) ~Hall term (4.5 mV/m, Figure 8g) + Electron pressure term (−1.4 mV/m, Figure 8a) within the error bars of ~1 mV/m for the electric field measurements. This allows us to consider that the measurements and calculations of different terms of the Ohm's law are reliable. One can notice that for both classes the ideal ion frozen-in condition is mostly broken along the N axis ($E'^i_N \sim 3$ mV/m, Figure 8d) whereas in contrast it is still well satisfied along L ($|E'^i_L| < 0.6$ mV/m, Figure 8b). This behavior is consistent with the idea of a front structure having a smaller (ion) scale in the direction of propagation (N) perpendicular to the background magnetic field than along it (L). However, a significant peak (both for median and average) of ($E'^i_M \sim 1.8$ mV/m, right-hand Figure 8c) is obtained for class II. This field is in the opposite direction of the M component of the Hall field (median value ~−1.6 mV/m, right-hand side Figure 8f) suggesting that the contribution from the electron pressure gradient would be quite large (~3.4 mV/m). As the median and mean values have opposite sign due to two extreme events, if we use the mean value (~+0.8 mV/m), the contribution of the electron pressure gradient would be only (~1 mV/m). These significant values of the electron pressure gradient along M could suggest that class II DFs have a smaller azimuthal scale (cross-tail direction) along M than class I DFs. Thus for both classes, in the N direction, ions are decoupled from the magnetic field mostly by the Hall electric field shown in Figure 8g. However, for class II and in the M direction, the electron pressure gradient could contribute significantly to ion decoupling. Furthermore, even in the N direction, the discrepancy between the two terms (ideal term and Hall field) can exceed $\simeq$ 1 mV/m. This excess statistically confirms that the electron pressure gradient term is not

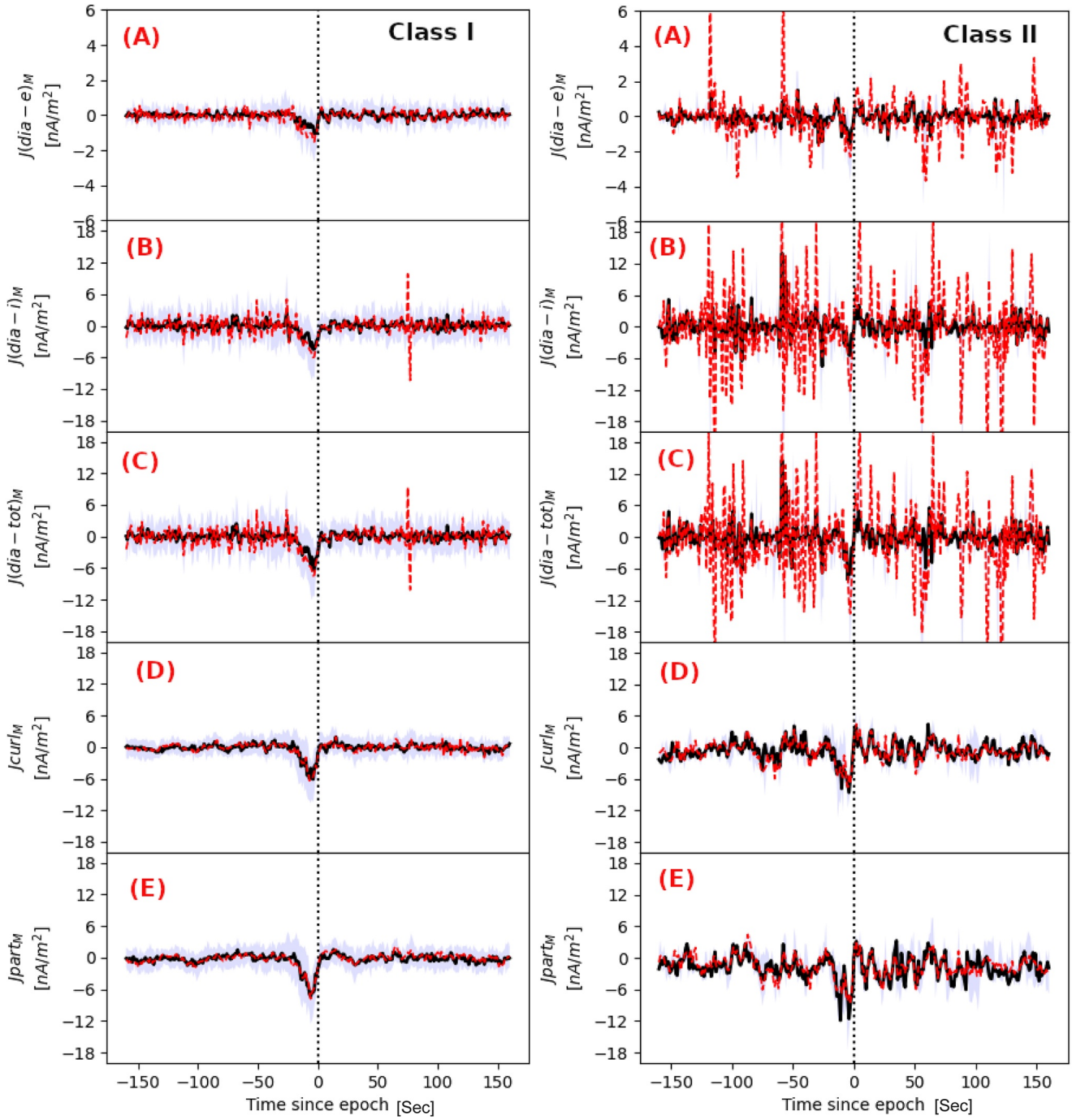

Figure 7. For both categories, superposed epoch analysis of the current densities along M calculated by using: (a) $J_{dia-e,M} = B_L/B^2\nabla_N P_e$, (b) $J_{dia-i,M} = B_L/B^2\nabla_N P_i$, (c) $J_{dia-tot,M} = B_L/B^2\nabla_N(P_e + P_i)$, (d) $\mathbf{J}_{\text{curl},M} = (\nabla \times \mathbf{B})/\mu_0$, and (e) $\mathbf{J}_{part,M} = en_e(\mathbf{v}_i - \mathbf{v}_e)$. Same color code as Figure 4.

negligible and reduce the positive Hall electric field along N despite the difficulty to estimate it from the four satellite measurements, see Figure 8a.

Figure 9 shows for both categories, the SEA of the ideal electron frozen-in term ($\mathbf{E'^e} = \mathbf{E} + \mathbf{v}_e \times \mathbf{B}$) in LMN coordinates. Both ions and electrons are mostly magnetized along the L direction (Figure 9b) as the ideal frozen-in term $|E'^e_L| < 0.8$ mV/m is about the electric field error bar although class II DFs are associated with larger fluctuations. In the N direction for class II DFs, electrons could be decoupled from the magnetic field as the departure to frozen-in condition ($E'^e_N \sim -1.6$ mV/m, right-hand side Figure 9d) is consistent with the estimated

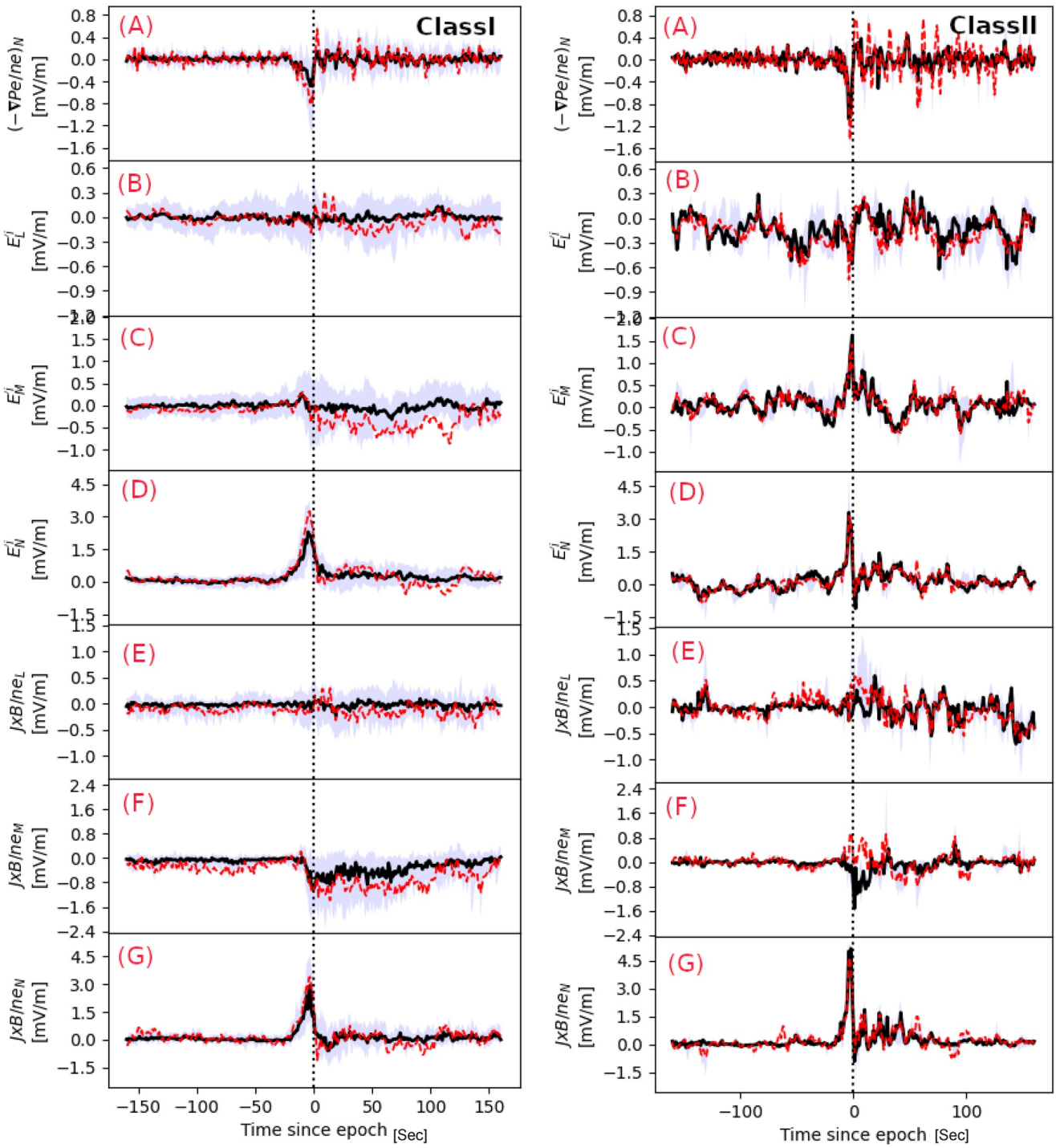

Figure 8. Superposed epoch analysis of the ion generalized Ohm's law comparison between different terms. Panel (a) includes the electron pressure gradient term along *N*. Panels (b–d) shows *L*, *M*, *N* components of the electric field $\mathbf{E}' = \mathbf{E} + \mathbf{v_i} \times \mathbf{B}$ and panels (e–g) shows *L*, *M*, *N* components of the Hall electric field $\mathbf{J}_{part}/(en_e)$, all data being time averaged at 0.3 s. Same color code as Figure 4.

electron pressure gradient term (right-hand side Figure 9a) and assuming a non-zero curl of the electron pressure gradient term $-(\nabla P_e)/(en_e)$. This agreement is also found for class I DFs showing a bipolar signature but with smaller values ($E_N'^e \sim \pm 0.8$ mV/m, left-hand side Figures 9a and 9d). In the *M* direction for which we are not able to estimate the electron pressure gradient, a larger departure to the ideal frozen-in condition is found for class II than for class I. This departure suggests, as from ion Ohm's law, that class II DFs could be more localized in the

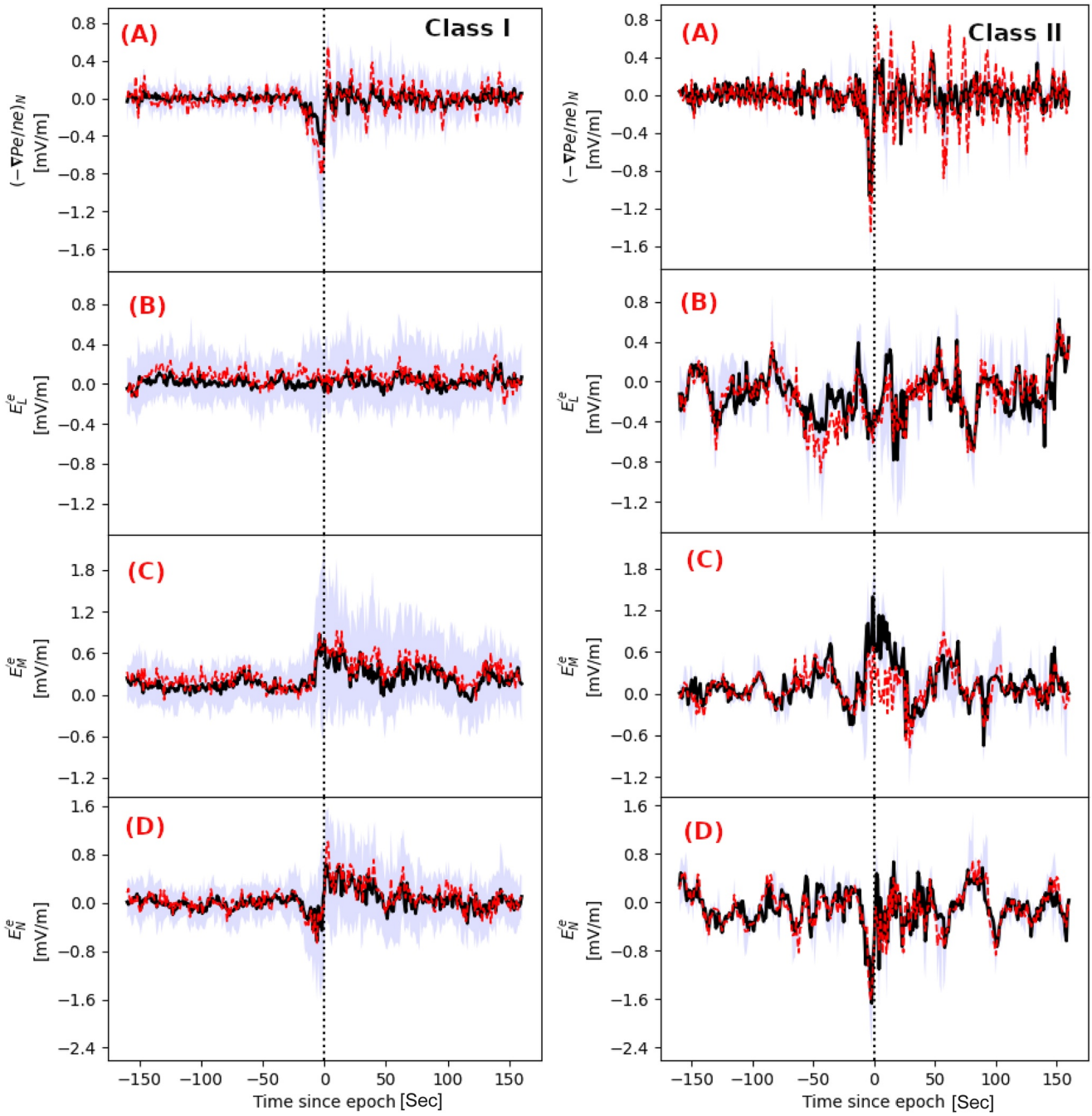

Figure 9. Superposed epoch analysis of the electron generalized Ohm's law comparison between different terms. Panel (a) includes the electron pressure gradient term along *N*. Panels (b–d) shows *L*, *M*, *N* components of the electric field $\mathbf{E}' = \mathbf{E} + \mathbf{v}_e \times \mathbf{B}$, all data being time averaged at 0.3 s. Same color code as Figure 4.

azimuthal (cross-tail) direction due to larger electron pressure gradients. Thus electrons could be decoupled from the magnetic field at DF by their pressure gradient term in the *N* direction and probably also in the *M* direction although it is not possible to confirm it using a single s/c method.

6. Energy Conversion at DF

In this section, we present the results from the SEA of the energy conversion processes. For energy conversion, positive values of $\mathbf{j} \cdot \mathbf{E}$ correspond to an energy load or dissipation whereas negative values correspond

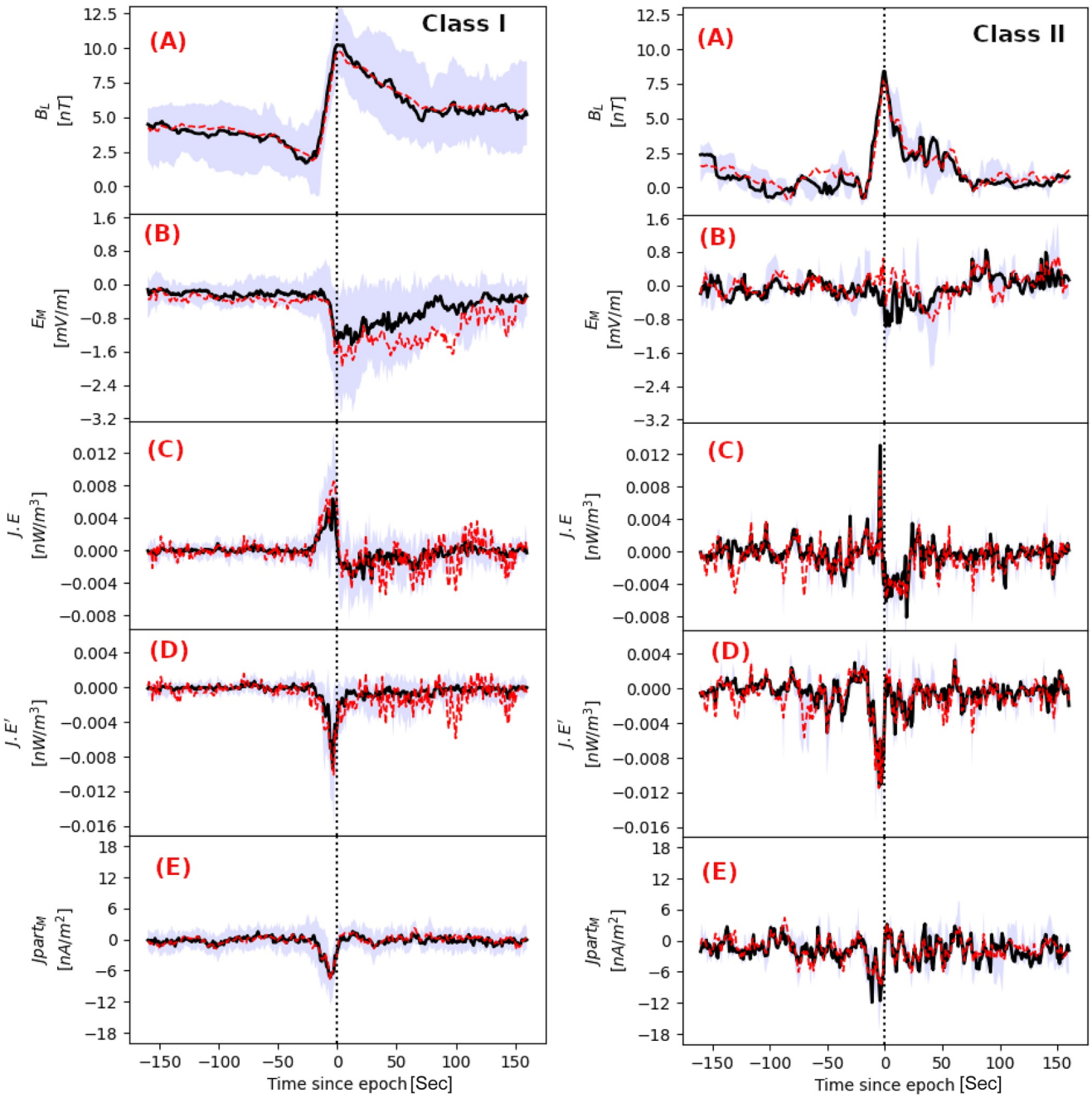

Figure 10. Superposed epoch analysis of the energy conversion processes. (a) The magnetic field B_L, (b) the electric field E_M, (c) the energy conversion term in s/c frame $\mathbf{j} \cdot \mathbf{E}$, (d) the energy conversion term in electron frame $\mathbf{j} \cdot (\mathbf{E} + \mathbf{v}_e \times \mathbf{B})$, and (e) the current density $Jpart_M$. Same color code as Figure 4.

to a generator or dynamo effect (e.g., Alqeeq et al., 2022; Birn & Hesse, 2005; Huang et al., 2015; Torbert et al., 2016). Figure 10 shows the results of the SEA of the energy conversion processes for our two DF categories. Figure 10a displays the magnetic component B_L for the context, Figure 10b the cross-tail electric field E_M, Figures 10c and 10d the energy conversion term in s/c frame $\mathbf{j} \cdot \mathbf{E}$ and in the electron frame $\mathbf{j} \cdot \mathbf{E}'$ respectively, and Figure 10e the current density $Jpart_M$ computed from particle measurements shown again for reference.For both categories, the SEA shows that, in the spacecraft frame Figure 10c, the energy is transferred from the electromagnetic fields to the plasma ($\mathbf{j} \cdot \mathbf{E} > 0$) ahead or at DF. This result is consistent with all previous DF studies. However, for class II as found for the six DF events by Alqeeq et al. (2022), a reversal of the energy conversion process is found behind the front. The energy is transferred from the plasma to the electromagnetic fields (**j**

$\cdot \mathbf{E} < 0$) due to the reversal of the ion diamagnetic current which has been confirmed in the previous section. Indeed, in Figure 10b, the M component of the electric field related to the fast convective earthward plasma motion does not change sign. Therefore, for both classes, the energy conversion processes in the vicinity of DFs seem to be governed by the ion pressure gradient generated by the flow propagation.

In the fluid frame Figure 10d, as found for the six DFs in Alqeeq et al. (2022), the statistical study confirms that for both classes the energy is transferred from the plasma to the electromagnetic fields ($\mathbf{J} \cdot \mathbf{E}' < 0$, generator or dynamo) due to the contribution of the electron pressure gradient in the Ohm's law and could lead to the slow down process of DFs during their earthward motion. Indeed, the thermal energy transport equation including the Joule term $\mathbf{J} \cdot \mathbf{E}'$ and the transport of the kinetic energy of the plasma bulk flow equation are coupled (e.g., Equations 10 and 11 Birn & Hesse, 2005). As in our six DF event study, we investigated the homogeneity of the energy conversion processes in the fluid frame observed around the DF. Indeed, from the six DF analysis which all belong to class II, we have shown that the energy conversion process is not homogeneous at the scale of the tetrahedron (electron scales). We have found strong variations of the sign and the amplitude of the energy conversion term obtained from one satellite to another. Such variations suggested that a physical process is going on at the electron scales while the DF is propagating earthward. Based on our estimates of the SD for each component of the current density and the electric field in the fluid frame ($\mathbf{E}' = \mathbf{E} + \mathbf{v}_e \times \mathbf{B}$) normalized by their respective error bar, which can be written as $\mathrm{SD}(X)/\Delta X = \sqrt{\Sigma_{i=1}^{4}(X_i - < X >)^2}/4/\Delta X$ where $< X >$ is the four spacecraft average of the X component and ΔX its respective estimated error bar, we have shown that the non homogeneity was caused mainly by the electric field fluctuations as discussed in Alqeeq et al. (2022) in detail. The SEA of the normalized SD of the electric field and the current density shown in Figure 11 confirms the dominant role of the electric field fluctuations in the variability of the energy conversion term. Indeed, for both classes, the SD of electric fields is about 1 for x and y components (Figures 11a and 11b) whereas the SD of current densities is always smaller than 1 for all components.

7. Summary and Discussion

We have reported on a statistical study based on 132 DFs detected by the MMS mission during the full magnetotail season of 2017 (end of April to end of August). We found that the 132 events can be subdivided into two categories mostly according to their DF-shape (magnetic field profile): class I with 98 events (74.4%) for which the DF-shape shows a slow decrease of the magnetic field after the DF and is associated with smaller ion velocity, class II with 34 events (25.6%) for which the DF-shape shows the same time scale for the rising and the falling of the magnetic field (a bump) associated with minimums of ion and electron pressures and faster velocity as shown in Alqeeq et al. (2022) for six DF events. These two classes can be considered as subcategories of the Schmid's DF category A (Schmid et al., 2015) as they both correspond to a decrease of the density and an increase of the temperature. Note that Schmid's DF category B was excluded of our selection by the criteria imposing a density decrease after the DF passage. Our two classes share the same property regarding the different sign of the magnetic dip preceding the DF as the two DF-dip subcategories identified by Schmid et al. (2019). However, our class II with negative dip has a larger median speed by a factor 2 than class I while Schmid's negative DF-dip subcategory only corresponds to an increase of 50% of their median speed compared with positive DF-dip subcategory. Furthermore, the bump profile of class II and its detection more located on the duskside are not found for their negative DF-dip subcategory. Finally, if their and our histograms of the radial distance of the DF location show that negative dip DFs are detected farther from the Earth (~25 R_E) than positive dip DFs (18 and 24 R_E in their study and ours, respectively), we do not find a decrease in class I DF with increasing distance from the Earth as the peak of their appearance is very close to that of class II DFs. Schmid et al. (2019) showed that the negative DF-dip category was correlated with field-aligned currents and suggested that they could correspond to flux rope structures and/or localized guide field reconnection events. However, from our study, we identified flux rope signatures usually ahead of DF and for both subcategories.

For both categories, using a single s/c method, we found that along the cross-tail current direction ($-M$), the ion diamagnetic current density contribution to the total diamagnetic current is dominant (~72%). For both categories, the enhancement of the ion pressure gradient ahead of the DF leads to an increase of the diamagnetic cross-tail current and to energy dissipation ($\mathbf{J} \cdot \mathbf{E} > 0$) in the spacecraft frame that is, an energy transfer from the electromagnetic field to the plasma. This result related to the DF contribution to the global energy dissipation process in the magnetosphere is consistent with previous statistical analysis (e.g., Song et al., 2020; Wang et al., 2020; Zhong et al., 2019). However, for our new class II, we have found a reversal of the energy conversion term. This reversal is mainly produced by the reversal of the ion pressure gradient that is, a reversal of their diamagnetic current as the main

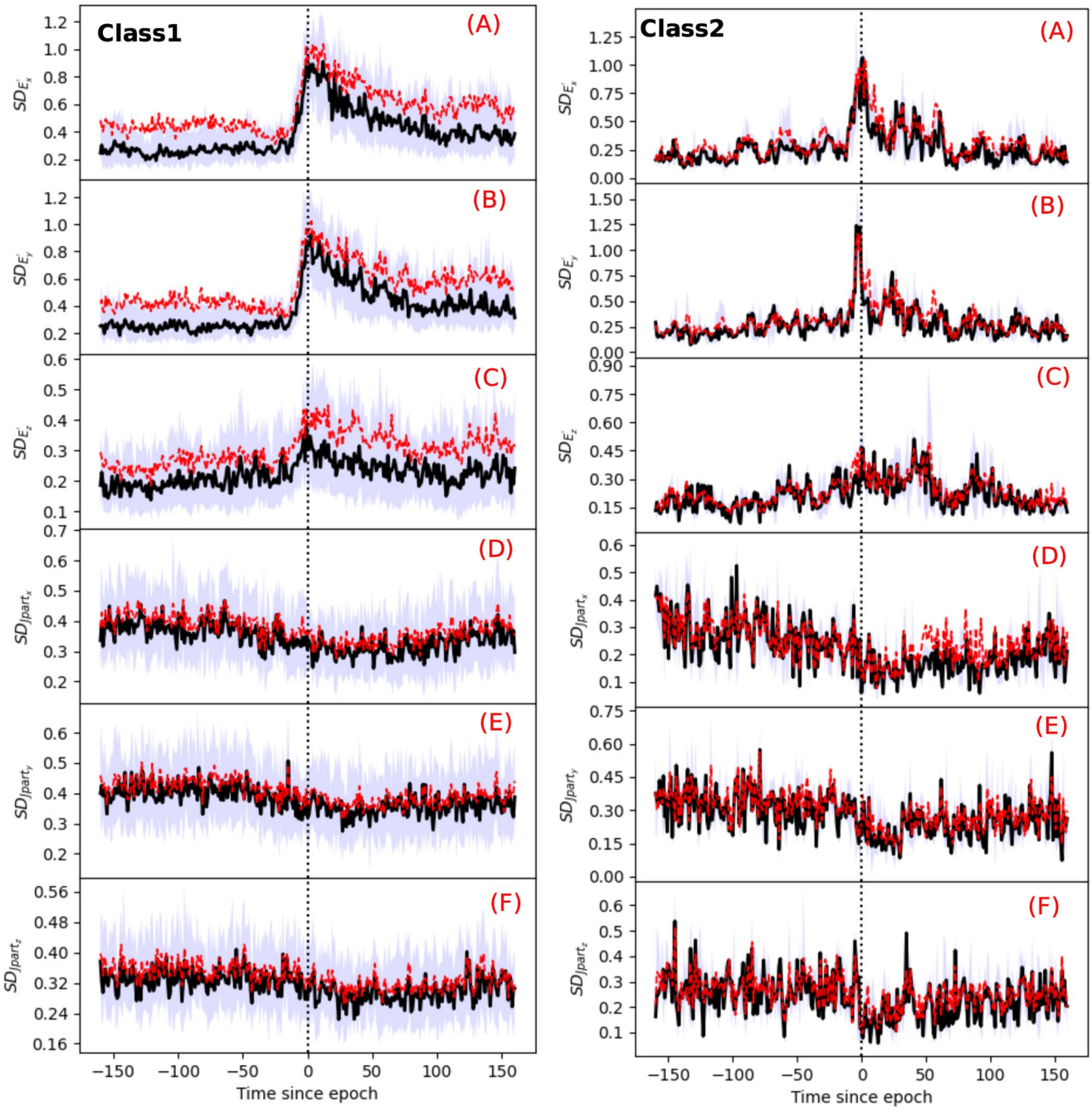

Figure 11. Superposed epoch analysis of the standard deviation of class I and class II for each component of the current density and the electric field in the fluid frame ($\mathbf{E}' = \mathbf{E} + \mathbf{v}_e \times \mathbf{B}$) in *GSE*, all data being time averaged at 0.3 s. For context, panel (a) the SD(E'_x), (b) the SD(E'_y), (c) the SD(E'_z), (d) the SD($Jpart_x$), (e) the SD($Jpart_y$), and (f) the SD($Jpart_z$). Same color code as Figure 4.

component along *M* of the electric field due to the fast earthward plasma motion does not change sign. Therefore for class II DF events, the energy is transferred from the plasma to the electromagnetic field behind the front ($\mathbf{J} \cdot \mathbf{E} < 0$, dynamo effect). This reversal of the energy conversion term with similar values raises the question of a net contribution to the energy dissipation from this class of DF which still represents about 1/4 of the DF events. It raises also the question about the cause of this different behavior compared with class I.

In the fluid frame and for both categories, we found that the energy is mostly transferred from the plasma to the electromagnetic field ($\mathbf{J} \cdot \mathbf{E}' < 0$) ahead or at the DF which could contribute to the deceleration of the flow.

As we have seen from the generalized Ohm's law analysis, the non-ideal electric field comes from the electron pressure gradient. The latter, although contributing little to the total diamagnetic current due to the lower temperature of electrons, could lead to the electron decoupling at the front (assuming that the electron pressure does not depend only on the density and a non-zero curl of the electron pressure gradient term $-(\nabla P_e)/(en_e)$), see Sittler and Scudder (1980)) for discussion and to a net energy conversion to the electromagnetic field. Thus, the energy conversion process in the vicinity of DFs seems to be mainly controlled by the particle pressure gradients: in the spacecraft frame, the contribution of the ion pressure gradient to the diamagnetic cross-tail current is dominant and determines the nature of the conversion process (dissipation vs. dynamo) as the motional electric field does not change sign; in the fluid frame the electron pressure gradient, although weaker than that of the ions due to the lower temperature of electrons, could be sufficient to lead to the decoupling of electrons and to a net energy transfer from the plasma to the electromagnetic field. This transfer could result to the slowdown of the fast flows.

Furthermore, we have shown that the SEA of the generalized Ohm's law for all events confirms that the ideal frozen-in condition is broken for ions mostly due to the Hall electric field ($\mathbf{J} \times \mathbf{B}/(en)$). We have seen that this field is produced by the enhancement of the cross-tail current caused by the ion pressure gradient at DF and the corresponding diamagnetic current but the electron pressure gradient although smaller also contributes. Electrons remain almost always magnetized except maybe at the front where a significant electron pressure gradient is found (assuming that the electron pressure does not depend only on the density). Finally, we have statistically examined the homogeneity of the energy conversion processes in the fluid frame by estimating the SD of the current density and of the electric field measurements. For both categories, we found that the non-homogeneity comes from the variations of the electric field which occur at electron (tetrahedron) scales. These variations are produced by variations in the electron pressure gradient which are likely caused by a kinetic scale process. From the six DF analysis, we have suggested that this process could be identified as the LHD instability whose energy source lies in the enhancement of the pressure gradient ahead of the front as reported from observations and simulations (e.g., Divin et al., 2015a, 2015b; Hosner et al., 2022; Sergeev et al., 2009).

The identification of the class II DFs raises many new questions:

- Why and how are they produced compared with the typical class I?
- Why are they mostly detected on the duskside?
- Why are they observed less often?
- What is their net contribution to the global circulation of magnetospheric energy?

We do not pretend here to answer all these new questions but we want to suggest some clues. The duskside near-Earth magnetotail (pre-midnight sector) has been known for a long time to be a preferential location for substorm onset (e.g., Angelopoulos et al., 2008, 2013; Baumjohann et al., 1999; Nagai et al., 1998) or/and magnetotail reconnection (e.g., Drake et al., 2014; H. S. Fu et al., 2013; Lu et al., 2019; Runov et al., 2012; Sitnov et al., 2009; M. Zhou et al., 2011). Therefore, class II DF events could be directly related to onset events although it has been shown that fast flows and DF can be detected without substorms (e.g., Lui, 2001; Runov et al., 2009, 2011). Class II DFs would be detected near the substorm onset with an higher probability in the pre-midnight sector but with a lower probability than fast flow detection anywhere across the magnetotail. This conjecture could be tested in the future by investigating the occurrence of substorm onset with regard to class II events.

Recently combining THEMIS observations and 3D PIC simulations, Panov et al. (2022) identified ion gyroradius scale structures associated with the propagation of heads produced by the non-linear evolution of the kinetic Ballooning-Interchange Instability (BICI). The BICI head structures correspond to the sharp increase of the northward component of the magnetic field and the decrease of the density (e.g., Pritchett et al., 2014). They were detected by the three THEMIS near-Earth probes when they were located between -7.5 and -7.9 R_E therefore much closer to the Earth than DFs detected by MMS. Their measurements were performed in a stronger magnetic field (~60 nT) and farther from the equator ($B_x \sim 40$ nT). Furthermore, the heads were moving dawnward while on each head side plasma was moving tailward leading to a flow reversal during the head crossing by the probes. However, some properties pointed out by Panov et al. (2022). could have some similarities with properties of class II DFs. The BICI head crossing is associated with a density trough and a hump of the ion temperature in addition to the classical DF signature (B_z increase up to 40 nT preceded by a negative dip and $V_x \sim 400$ km/s) as for class II. The authors used the spacecraft potential with a time resolution of 1/128 ~ 0.008 s to estimate the density and to show the density trough. As THEMIS spin resolution (3 s) of particle moments is not sufficient. Moreover, while from THEMIS measurements the authors showed that the ion temperature increases by a factor

2 on the duskside of the head, in our MMS measurements we found only an increase ∼50%. They attributed the enhancement of the ion temperature on the duskside of the head to the penetration of the suprathermal ions from the dawnside across the head to the duskside. This process could be also investigated in the future from our DF database. Despite these differences, BICI head crossing appears to be a good candidate to interpret our class II DFs. However taking into account the different locations between THEMIS and MMS observations, class II DFs could correspond to BICI head crossings in the early stages of their development before they were slowed down and broadened closer to the Earth due to the interaction with the stronger dipole field.

8. Conclusion

From a statistical study based on MMS data gathered during the full magnetotail season of 2017, we have identified two DF subcategories mostly according to their DF-shape (magnetic field profile): class I (74.4%) showing a slow decrease of the magnetic field after the DF and associated with smaller ion velocity, class II (25.6%) showing the same time scale for the rising and the falling of the magnetic field (a bump) associated with minimums of ion and electron pressures and faster velocity. For both categories, the ion diamagnetic current density contribution to the total diamagnetic current is dominant (∼72%) and lead to an energy dissipation ($\mathbf{J}\cdot\mathbf{E} > 0$) ahead of the DF that is, an energy transfer from the electromagnetic field to the plasma. However, class II presents a reversal of the energy conversion term after the DF. This reversal is mainly produced by the reversal of the ion pressure gradient that is, a reversal of their diamagnetic current as the main component along M of the electric field due to the fast earthward plasma motion does not change sign. Therefore, the energy is transferred from the plasma to the electromagnetic field behind the front ($\mathbf{J}\cdot\mathbf{E} < 0$, dynamo effect). In the fluid frame and for both categories, we found that the energy is mostly transferred from the plasma to the electromagnetic field ($\mathbf{J}\cdot\mathbf{E}' < 0$) ahead or at the DF which could contribute to the deceleration of the flow. For both categories, we found that this energy conversion is not homogeneous at the electron scale due to the electric field variations which could be related to the growth of lower-hybrid waves from the DF density gradient (e.g., Divin et al., 2015a, 2015b; Hosner et al., 2022; Sergeev et al., 2009). Ions are found to be decoupled from the magnetic field along the normal direction at DF mainly due to the Hall electric field although the electron pressure could contribute too. Electrons could be also decoupled at DF by the effect of their electron pressure gradient assuming a non-zero curl of the electron pressure gradient term $-(\nabla P_e)/(en_e)$, that is, a pressure not depending only on the density. Although sharing common properties with the two subcategories identified by Schmid et al. (2019) based on the sign of the magnetic dip preceding the DF, our classe II DF shows important distinct features: a magnetic bump profile, faster speed and location on the duskside. Schmid et al. (2019) suggested that their negative dip DF events could be related to flux ropes or localized reconnection events with guide field. Although our study does not rule out these suggestions, we did not find more flux rope signatures associated with our class II than class I. We suggest that class II DF events could be also related to BICI head crossings described by Panov et al. (2022). Further investigations are therefore still necessary to better understand the nature and the contribution to the global energy cycle of the different classes of DFs moving toward the Earth through the magnetotail.

Data Availability Statement

The data set used in the present study is collected by the NASA' MMS mission and is publicly available at (https://lasp.colorado.edu/mms/sdc/public/about/browse-wrapper/). The Space Physics Environment Data Analysis Software framework (SPEDAS, http://spedas.org/), an Artificial Intelligence Data Analysis (AIDApy, https://aidapy.readthedocs.io/en/latest/), and the State Estimation and Analysis in Python (SeaPy, https://spacepy.github.io/seapy.html) were used to analyze and plot the data.

Acknowledgments
We thank the entire MMS team for providing data publicly available from the MMS Science Data Center (http://lasp.colorado.edu/mms/sdc/public/), the spedas software team (Angelopoulos et al., 2019) in particular E. Grimes for pyspedas effort developments, the AIDApy software team (Lapenta & AIDA H2020 Team, 2019), and the SeaPy software team (Morley et al., 2014). S.W. Alqeeq's PhD fellowship is supported by CNES and PAUSE program (https://www.college-de-france.fr/site/programme-pause/index.htm), managed by CNRS.

References

Alqeeq, S. W., Le Contel, O., Canu, P., Retinò, A., Chust, T., Mirioni, L., et al. (2022). Investigation of the homogeneity of energy conversion processes at dipolarization fronts from MMS measurements. *Physics of Plasmas*, *29*(1), 012906. https://doi.org/10.1063/5.0069432

Angelopoulos, V. (2008). The THEMIS mission. *Space Science Reviews*, *141*(1–4), 5–34. https://doi.org/10.1007/s11214-008-9336-1

Angelopoulos, V., Baumjohann, W., Kennel, C. F., Coronti, F. V., Kivelson, M. G., Pellat, R., et al. (1992). Bursty bulk flows in the inner Central plasma sheet. *Journal of Geophysical Research*, *97*(A4), 4027–4039. https://doi.org/10.1029/91JA02701

Angelopoulos, V., Cruce, P., Drozdov, A., Grimes, E. W., Hatzigeorgiu, N., King, D. A., et al. (2019). The space physics environment data analysis system (SPEDAS). *Space Science Reviews*, *215*(1), 9. https://doi.org/10.1007/s11214-018-0576-4

Angelopoulos, V., Kennel, C. F., Coroniti, F. V., Pellat, R., Kivelson, M. G., Walker, R. J., et al. (1994). Statistical characteristics of bursty bulk flow events. *Journal of Geophysical Research*, *99*(A11), 21257–21280. https://doi.org/10.1029/94JA01263

Angelopoulos, V., McFadden, J. P., Larson, D., Carlson, C. W., Mende, S. B., Frey, H., et al. (2008). Tail reconnection triggering substorm onset. *Science*, *321*(5891), 931–935. https://doi.org/10.1126/science.1160495

Angelopoulos, V., Runov, A., Zhou, X. Z., Turner, D. L., Kiehas, S. A., Li, S. S., & Shinohara, I. (2013). Electromagnetic energy conversion at reconnection fronts. *Science*, *341*(6153), 1478–1482. https://doi.org/10.1126/science.1236992

Baumjohann, W., Hesse, M., Kokubun, S., Mukai, T., Nagai, T., & Petrukovich, A. A. (1999). Substorm dipolarization and recovery. *Journal of Geophysical Research*, *104*(A11), 24995–25000. https://doi.org/10.1029/1999JA900282

Baumjohann, W., Paschmann, G., & Luehr, H. (1990). Characteristics of high-speed ion flows in the plasma sheet. *Journal of Geophysical Research*, *95*(A4), 3801–3809. https://doi.org/10.1029/JA095iA04p03801

Birn, J., & Hesse, M. (2005). Energy release and conversion by reconnection in the magnetotail. *Annales Geophysicae*, *23*(10), 3365–3373. https://doi.org/10.5194/angeo-23-3365-2005

Burch, J. L., Torbert, R. B., Phan, T. D., Chen, L.-J., Moore, T. E., Ergun, R. D., et al. (2016). Electron-scale measurements of magnetic reconnection in space. *Science*, *352*(6290), aaf2939. https://doi.org/10.1126/science.aaf2939

Chanteur, G., & Harvey, C. (1998). Spatial interpolation fo four spacecraft: Application to magnetic gradients. In G. Paschman & P. Daly (Eds.), *Analysis methods for multi-spacecraft data* (pp. 371–393). European Space Agency.

Divin, A., Khotyaintsev, Y. V., Vaivads, A., & André, M. (2015a). Lower hybrid drift instability at a dipolarization front. *Journal of Geophysical Research: Space Physics*, *120*(2), 1124–1132. https://doi.org/10.1002/2014JA020528

Divin, A., Khotyaintsev, Y. V., Vaivads, A., André, M., Markidis, S., & Lapenta, G. (2015b). Evolution of the lower hybrid drift instability at reconnection jet front. *Journal of Geophysical Research: Space Physics*, *120*(4), 2675–2690. https://doi.org/10.1002/2014JA020503

Drake, J. F., Swisdak, M., Cassak, P. A., & Phan, T. D. (2014). On the 3-D structure and dissipation of reconnection-driven flow bursts. *Geophysical Research Letters*, *41*(11), 3710–3716. https://doi.org/10.1002/2014GL060249

Ergun, R. E., Goodrich, K. A., Stawarz, J. E., Andersson, L., & Angelopoulos, V. (2015). Large-amplitude electric fields associated with bursty bulk flow braking in the Earth's plasma sheet. *Journal of Geophysical Research: Space Physics*, *120*(3), 1832–1844. https://doi.org/10.1002/2014JA020165

Ergun, R. E., Tucker, S., Westfall, J., Goodrich, K. A., Malaspina, D. M., Summers, D., et al. (2016). The axial double probe and fields signal processing for the MMS mission. *Space Science Reviews*, *199*(1–4), 167–188. https://doi.org/10.1007/s11214-014-0115-x

Escoubet, C. P., Fehringer, M., & Goldstein, M. L. (2001). Introduction the cluster mission. *Annales Geophysicae*, *19*(10/12), 1197–1200. https://doi.org/10.5194/angeo-19-1197-2001

Fu, H., Grigorenko, E. E., Gabrielse, C., Liu, C., Lu, S., Hwang, K. J., et al. (2020). Magnetotail dipolarization fronts and particle acceleration: A review. *Science China Earth Sciences*, *63*(2), 235–256. https://doi.org/10.1007/s11430-019-9551-y

Fu, H. S., Cao, J. B., Khotyaintsev, Y. V., Sitnov, M. I., Runov, A., Fu, S. Y., et al. (2013). Dipolarization fronts as a consequence of transient reconnection: In situ evidence. *Geophysical Research Letters*, *40*(23), 6023–6027. https://doi.org/10.1002/2013GL058620

Fu, H. S., Khotyaintsev, Y. V., André, M., & Vaivads, A. (2011). Fermi and betatron acceleration of suprathermal electrons behind dipolarization fronts. *Geophysical Research Letters*, *38*(16), L16104. https://doi.org/10.1029/2011GL048528

Fu, H. S., Khotyaintsev, Y. V., Vaivads, A., André, M., & Huang, S. Y. (2012a). Electric structure of dipolarization front at sub-proton scale. *Geophysical Research Letters*, *39*(6), L06105. https://doi.org/10.1029/2012GL051274

Fu, H. S., Khotyaintsev, Y. V., Vaivads, A., André, M., Sergeev, V. A., Huang, S. Y., et al. (2012b). Pitch angle distribution of suprathermal electrons behind dipolarization fronts: A statistical overview. *Journal of Geophysical Research*, *117*(A12), A12221. https://doi.org/10.1029/2012JA018141

Hamrin, M., Pitkänen, T., Norqvist, P., Karlsson, T., Nilsson, H., André, M., et al. (2014). Evidence for the braking of flow bursts as they propagate toward the Earth. *Journal of Geophysical Research: Space Physics*, *119*(11), 9004–9018. https://doi.org/10.1002/2014JA020285

Hosner, M., Nakamura, R., Nakamura, T. K. M., Schmid, D., Panov, E. V., & Plaschke, F. (2022). Statistical investigation of electric field fluctuations around the lower-hybrid frequency range at dipolarization fronts in the near-earth magnetotail. *Physics of Plasmas*, *29*(1), 012111. https://doi.org/10.1063/5.0067382

Huang, S. Y., Fu, H. S., Yuan, Z. G., Zhou, M., Fu, S., Deng, X. H., et al. (2015). Electromagnetic energy conversion at dipolarization fronts: Multispacecraft results. *Journal of Geophysical Research: Space Physics*, *120*(6), 4496–4502. https://doi.org/10.1002/2015JA021083

Khotyaintsev, Y. V., Divin, A., Vaivads, A., André, M., & Markidis, S. (2017). Energy conversion at dipolarization fronts. *Geophysical Research Letters*, *44*(3), 1234–1242. https://doi.org/10.1002/2016GL071909

Lapenta, G., & AIDA H2020 Team. (2019). Processing big data from space missions and massively parallel simulations within the Horizon 2020 Project AIDA. In *Solar heliospheric and interplanetary environment* (p. 44).

Le Contel, O., Nakamura, R., Breuillard, H., Argall, M. R., Graham, D. B., Fischer, D., et al. (2017). Lower hybrid drift waves and electromagnetic electron space-phase holes associated with dipolarization fronts and field-aligned currents observed by the Magnetospheric Multiscale mission during a substorm. *Journal of Geophysical Research: Space Physics*, *122*(12), 12236–12257. https://doi.org/10.1002/2017JA024550

Li, H., Zhou, M., Deng, X., Yuan, Z., Guo, L., Yu, X., et al. (2015). A statistical study on the whistler waves behind dipolarization fronts. *Journal of Geophysical Research: Space Physics*, *120*(2), 1086–1095. https://doi.org/10.1002/2014JA020474

Li, J.-Z., Zhou, X.-Z., Angelopoulos, V., Liu, J., Runov, A., Pan, D.-X., & Zong, Q.-G. (2016). Contribution of ion reflection to the energy budgets of dipolarization fronts. *Geophysical Research Letters*, *43*(2), 493–500. https://doi.org/10.1002/2015GL067300

Lindqvist, P.-A., Olsson, G., Torbert, R. B., King, B., Granoff, M., Rau, D., et al. (2016). The spin-plane double probe electric field instrument for MMS. *Space Science Reviews*, *199*(1–4), 137–165. https://doi.org/10.1007/s11214-014-0116-9

Liu, C. M., Fu, H. S., Xu, Y., Khotyaintsev, Y. V., Burch, J. L., Ergun, R. E., et al. (2018). Electron-scale measurements of dipolarization front. *Geophysical Research Letters*, *45*(10), 4628–4638. https://doi.org/10.1029/2018GL077928

Liu, J., Angelopoulos, V., Runov, A., & Zhou, X.-Z. (2013). On the current sheets surrounding dipolarizing flux bundles in the magnetotail: The case for wedgelets. *Journal of Geophysical Research: Space Physics*, *118*(5), 2000–2020. https://doi.org/10.1002/jgra.50092

Lu, S., Artemyev, A. V., Angelopoulos, V., Lin, Y., Zhang, X. J., Liu, J., et al. (2019). The Hall electric field in Earth's magnetotail thin current sheet. *Journal of Geophysical Research: Space Physics*, *124*(2), 1052–1062. https://doi.org/10.1029/2018JA026202

Lui, A. T. Y. (2001). Current controversies in magnetospheric physics. *Reviews of Geophysics*, *39*(4), 535–563. https://doi.org/10.1029/2000RG000090

Morley, S., Koller, J., Welling, D., Larsen, B., & Niehof, J. (2014). *SpacePy*. Python-Based Tools for the Space Science Community.

Nagai, T., Fujimoto, M., Saito, Y., Machida, S., Terasawa, T., Nakamura, R., et al. (1998). Structure and dynamics of magnetic reconnection for substorm onsets with Geotail observations. *Journal of Geophysical Research*, *103*(A3), 4419–4440. https://doi.org/10.1029/97JA02190

Nakamura, R., Baumjohann, W., Mouikis, C., Kistler, L. M., Runov, A., Volwerk, M., et al. (2004). Spatial scale of high-speed flows in the plasma sheet observed by Cluster. *Geophysical Research Letters*, *31*(9), L09804. https://doi.org/10.1029/2004GL019558

Nakamura, T. K. M., Umeda, T., Nakamura, R., Fu, H. S., & Oka, M. (2019). Disturbance of the front region of magnetic reconnection outflow Jets due to the lower-hybrid drift instability. *Physical Review Letters*, *123*(23), 235101. https://doi.org/10.1103/PhysRevLett.123.235101

Ohtani, S.-I., Shay, M. A., & Mukai, T. (2004). Temporal structure of the fast convective flow in the plasma sheet: Comparison between observations and two-fluid simulations. *Journal of Geophysical Research*, *109*(A3), A03210. https://doi.org/10.1029/2003JA010002

Pan, D.-X., Khotyaintsev, Y. V., Graham, D. B., Vaivads, A., Zhou, X.-Z., André, M., et al. (2018). Rippled electron-scale structure of a dipolarization front. *Geophysical Research Letters*, *45*(22), 12116–12124. https://doi.org/10.1029/2018GL080826

Pan, D.-X., Zhou, X.-Z., Shi, Q.-Q., Liu, J., Angelopoulos, V., Runov, A., et al. (2015). On the generation of magnetic dips ahead of advancing dipolarization fronts. *Geophysical Research Letters*, *42*(11), 4256–4262. https://doi.org/10.1002/2015GL064369

Panov, E. V., Lu, S., & Pritchett, P. L. (2022). Magnetotail ion structuring by kinetic ballooning-interchange instability. *Geophysical Research Letters*, *49*(3), e96796. https://doi.org/10.1029/2021GL096796

Pollock, C., Moore, T., Jacques, A., Burch, J., Gliese, U., Saito, Y., et al. (2016). Fast plasma investigation for magnetospheric Multiscale. *Space Science Reviews*, *199*(1–4), 331–406. https://doi.org/10.1007/s11214-016-0245-4

Pontius, J. D. H., & Wolf, R. A. (1990). Transient flux tubes in the terrestrial magnetosphere. *Geophysical Research Letters*, *17*(1), 49–52. https://doi.org/10.1029/GL017i001p00049

Pritchett, P. L., & Coroniti, F. V. (2010). A kinetic ballooning/interchange instability in the magnetotail. *Journal of Geophysical Research*, *115*(A6), A06301. https://doi.org/10.1029/2009JA014752

Pritchett, P. L., Coroniti, F. V., & Nishimura, Y. (2014). The kinetic ballooning/interchange instability as a source of dipolarization fronts and auroral streamers. *Journal of Geophysical Research: Space Physics*, *119*(6), 4723–4739. https://doi.org/10.1002/2014JA019890

Richard, L., Khotyaintsev, Y. V., Graham, D. B., & Russell, C. T. (2022). Are dipolarization fronts a typical feature of magnetotail plasma jets fronts? *Geophysical Research Letters*, *49*(22), e2022GL101693. https://doi.org/10.1029/2022GL101693

Runov, A., Angelopoulos, V., Sitnov, M. I., Sergeev, V. A., Bonnell, J., McFadden, J. P., et al. (2009). THEMIS observations of an earthward-propagating dipolarization front. *Geophysical Research Letters*, *36*(14), L14106. https://doi.org/10.1029/2009GL038980

Runov, A., Angelopoulos, V., & Zhou, X. Z. (2012). Multipoint observations of dipolarization front formation by magnetotail reconnection. *Journal of Geophysical Research*, *117*(A5), A05230. https://doi.org/10.1029/2011JA017361

Runov, A., Angelopoulos, V., Zhou, X. Z., Zhang, X. J., Li, S., Plaschke, F., & Bonnell, J. (2011). A THEMIS multicase study of dipolarization fronts in the magnetotail plasma sheet. *Journal of Geophysical Research*, *116*(A5), A05216. https://doi.org/10.1029/2010JA016316

Russell, C. T., Anderson, B. J., Baumjohann, W., Bromund, K. R., Dearborn, D., Fischer, D., et al. (2016). The magnetospheric multiscale magnetometers. *Space Science Reviews*, *199*(1–4), 189–256. https://doi.org/10.1007/s11214-014-0057-3

Schmid, D., Nakamura, R., Plaschke, F., Volwerk, M., & Baumjohann, W. (2015). Two states of magnetotail dipolarization fronts: A statistical study. *Journal of Geophysical Research: Space Physics*, *120*(2), 1096–1108. https://doi.org/10.1002/2014JA020380

Schmid, D., Volwerk, M., Nakamura, R., Baumjohann, W., & Heyn, M. (2011). A statistical and event study of magnetotail dipolarization fronts. *Annales Geophysicae*, *29*(9), 1537–1547. https://doi.org/10.5194/angeo-29-1537-2011

Schmid, D., Volwerk, M., Plaschke, F., Nakamura, R., Baumjohann, W., Wang, G. Q., et al. (2019). A statistical study on the properties of dips ahead of dipolarization fronts observed by MMS. *Journal of Geophysical Research: Space Physics*, *124*(1), 139–150. https://doi.org/10.1029/2018JA026062

Sergeev, V., Angelopoulos, V., Apatenkov, S., Bonnell, J., Ergun, R., Nakamura, R., et al. (2009). Kinetic structure of the sharp injection/dipolarization front in the flow-braking region. *Geophysical Research Letters*, *36*(21), L21105. https://doi.org/10.1029/2009GL040658

Sitnov, M. I., Merkin, V. G., Roytershteyn, V., & Swisdak, M. (2018). Kinetic dissipation around a dipolarization front. *Geophysical Research Letters*, *45*(10), 4639–4647. https://doi.org/10.1029/2018GL077874

Sitnov, M. I., Swisdak, M., & Divin, A. V. (2009). Dipolarization fronts as a signature of transient reconnection in the magnetotail. *Journal of Geophysical Research*, *114*(A4), A04202. https://doi.org/10.1029/2008JA013980

Sittler, J. E. C., & Scudder, J. D. (1980). An empirical polytrope law for solar wind thermal electrons between 0.45 and 4.76 AU: Voyager 2 and Mariner 10. *Journal of Geophysical Research*, *85*(A10), 5131–5137. https://doi.org/10.1029/JA085iA10p05131

Song, L., Zhou, M., Yi, Y., Deng, X., Zhong, Z., & Man, H. (2020). Force and energy balance of the dipolarization front. *Journal of Geophysical Research: Space Physics*, *125*(9), e28278. https://doi.org/10.1029/2020JA028278

Sonnerup, B. U. Ö., & Scheible, M. (1998). Minimum and maximum variance analysis. *ISSI Scientific Reports Series*, *1*, 185–220.

Stawarz, J. E., Ergun, R. E., & Goodrich, K. A. (2015). Generation of high-frequency electric field activity by turbulence in the Earth's magnetotail. *Journal of Geophysical Research: Space Physics*, *120*(3), 1845–1866. https://doi.org/10.1002/2014JA020166

Torbert, R. B., Russell, C. T., Magnes, W., Ergun, R. E., Lindqvist, P.-A., LeContel, O., et al. (2016). The FIELDS instrument suite on MMS: Scientific objectives, measurements, and data products. *Space Science Reviews*, *199*(1–4), 105–135. https://doi.org/10.1007/s11214-014-0109-8

Wang, L., Huang, C., Cao, X., Du, A., & Ge, Y. S. (2020). Magnetic energy conversion and transport in the terrestrial magnetotail due to dipolarization fronts. *Journal of Geophysical Research: Space Physics*, *125*(10), e28568. https://doi.org/10.1029/2020JA028568

Wolf, R. A., Wan, Y., Xing, X., Zhang, J. C., & Sazykin, S. (2009). Entropy and plasma sheet transport. *Journal of Geophysical Research*, *114*(A9), A00D05. https://doi.org/10.1029/2009JA014044

Yang, J., Cao, J. B., Fu, H. S., Wang, T. Y., Liu, W. L., & Yao, Z. H. (2017). Broadband high-frequency waves detected at dipolarization fronts. *Journal of Geophysical Research: Space Physics*, *122*(4), 4299–4307. https://doi.org/10.1002/2016JA023465

Yang, Y., Matthaeus, W. H., Parashar, T. N., Haggerty, C. C., Roytershteyn, V., Daughton, W., et al. (2017). Energy transfer, pressure tensor, and heating of kinetic plasma. *Physics of Plasmas*, *24*(7), 072306. https://doi.org/10.1063/1.4990421

Yao, Z., Sun, W. J., Fu, S. Y., Pu, Z. Y., Liu, J., Angelopoulos, V., et al. (2013). Current structures associated with dipolarization fronts. *Journal of Geophysical Research: Space Physics*, *118*(11), 6980–6985. https://doi.org/10.1002/2013JA019290

Yao, Z. H., Liu, J., Owen, C. J., Forsyth, C., Rae, I. J., Pu, Z. Y., et al. (2015). A physical explanation for the magnetic decrease ahead of dipolarization fronts. *Annales Geophysicae*, *33*(10), 1301–1309. https://doi.org/10.5194/angeo-33-1301-2015

Yao, Z. H., Rae, I. J., Guo, R. L., Fazakerley, A. N., Owen, C. J., Nakamura, R., et al. (2017). A direct examination of the dynamics of dipolarization fronts using MMS. *Journal of Geophysical Research: Space Physics*, *122*(4), 4335–4347. https://doi.org/10.1002/2016JA023401

Young, D. T., Burch, J. L., Gomez, R. G., De Los Santos, A., Miller, G. P., Wilson, P., et al. (2016). Hot plasma composition analyzer for the Magnetospheric Multiscale mission. *Space Science Reviews*, *199*(1–4), 407–470. https://doi.org/10.1007/s11214-014-0119-6

Zhong, Z. H., Deng, X. H., Zhou, M., Ma, W. Q., Tang, R. X., Khotyaintsev, Y. V., et al. (2019). Energy conversion and dissipation at dipolarization fronts: A statistical overview. *Geophysical Research Letters*, *46*(22), 12693–12701. https://doi.org/10.1029/2019GL085409

Zhou, M., Huang, S.-Y., Deng, X.-H., & Pang, Y. (2011). Observation of a sharp negative dipolarization front in the reconnection outflow region. *Chinese Physics Letters*, *28*(10), 109402. https://doi.org/10.1088/0256-307X/28/10/109402

Zhou, X.-Z., Angelopoulos, V., Liu, J., Runov, A., & Li, S. S. (2014). On the origin of pressure and magnetic perturbations ahead of dipolarization fronts. *Journal of Geophysical Research: Space Physics*, *119*(1), 211–220. https://doi.org/10.1002/2013JA019394